ChemMedChem

Research Article
doi.org/10.1002/cmdc.202300046

Chemistry
Europe
European Chemical
Societies Publishing

www.chemmedchem.org

Scouting Different Phosphodiesterase 4 Inhibitor Chemotypes in Silico To Guide the Design of Anti-inflammatory/Antioxidant Agents

Elena Cichero,[a] Federica Rapetti,[a] Matteo Lusardi,[a] Naomi Scarano,[a] Silvana Alfei,[b] Paola Altieri,[c] Silvano Garibaldi,[c] Pietro Ameri,[c] Maria Grazia Signorello,[d] and Chiara Brullo*[a]

During the last years, we developed a large library of new selective phosphodiesterase 4D inhibitors, maintaining the catechol portion of the well-known PDE4 inhibitor Rolipram, featuring different substitutions in place of the lactam group of this reference compound. Based on the X-ray analysis of PDE4 inhibitors (PDE4Is) previously synthesized by us and of naphthyridine- and naphthyridinone-containing derivatives exhibiting PDE4 inhibitory ability described in the literature, we designed and synthesized new compounds **1–3**. All of them were screened in silico as putative PDE4Is, via molecular docking studies to exploit structural variation at the catechol group to gain further contacts especially with the flat aromatic residues (Phe506 and Phe538) of enzyme. Subsequent in silico prediction of ADMET properties and in vitro biological assays on platelets and endothelial cells are in good agreement with our previous data concerning the antioxidant/anti-inflammatory activity exhibited by our previous PDE4Is and similarly to other well-known PDE4Is.

Introduction

The second messenger, 3′,5′-cyclic adenosine monophosphate (cAMP) plays a key role in different biochemical processes,[1] representing a key intracellular modulator, particularly in inflammation.[2,3] Control of cAMP degradation in cells is regulated by a family of enzymes called phosphodiesterases (PDEs).[4] Since PDEs metabolize cAMP, related phosphodiesterase inhibitors (PDEIs) are thought to contrast the cAMP degradation counteracting inflammatory events. In this context,

the PDE4 isoenzyme is highly expressed in neurons, inflammatory and epithelial cells, and is involved in pulmonary, dermatological, and central nervous system diseases. In fact, PDE4Is show anti-inflammatory ability in pre-clinical models relevant to chronic obstructive pulmonary disease (COPD),[5–7] psoriasis,[8] and in neuro-inflammation related disorders as multiple sclerosis.[9] PDE4 has four isotypes, PDE4A-D. Initially, PDE4B was reported as linked to anti-inflammatory role, while the PDE4I side effects, as vomiting, nausea, sedation and gastroesophageal reflexes, were attributed to PDE4D.[10–12] In fact, has been clearly demonstrated that the PDE4 isoforms evidenced different cellular expression and compartmentalization, offering an efficacious targeted approach to treat neuro-inflammatory diseases, avoiding side effects.[13] During the last years, several X-ray crystallography experiments revealed that the four PDE4 isoforms show little difference at their catalytic domains,[10,14] making the search of dual PDE4B/D inhibitors conceivably effective and viable, more than that the discovery of isoform-selective compounds. Studies reported by Card[15] described the enzyme active site as subdivided into three pockets: a metal binding pocket (M pocket); a solvent filled side pocket (S pocket); and a pocket containing the purine-selective glutamine and the hydrophobic clamp (Q pocket). While M pocket contains metal ions and several highly conserved hydrophobic and polar residues, the S pocket includes hydrophilic amino acids which are solved by a network of water molecules in most of the collected X-ray data. Then, the Q pocket consists of the conserved glutamine residue involved in the inhibitor binding, as well as several hydrophobic amino acids. A comparison of the main residues belonging to the previously cited M, S and Q pockets at the PDE4B and PDE4D proteins are shown in Supporting Information, Table S1.

[a] Prof. E. Cichero, Dr. F. Rapetti, Dr. M. Lusardi, Dr. N. Scarano, Prof. C. Brullo
Department of Pharmacy (DIFAR)
Section of Medicinal Chemistry
University of Genova
Viale Benedetto XV 3, 16132 Genova (Italy)
E-mail: chiara.brullo@unige.it

[b] S. Alfei
Department of Pharmacy (DIFAR)
Section of Organic Chemistry
University of Genova
Viale Cembrano 4, 16148 Genova (Italy)

[c] P. Altieri, S. Garibaldi, P. Ameri
Department of Internal Medicine
School of Medical and Pharmaceutical Sciences
University of Genova
Viale Benedetto XV 3, 16132 Genova (Italy)

[d] M. Grazia Signorello
Department of Pharmacy
Biochemistry Lab
University of Genova
Viale Benedetto XV 3, 16132 Genova (Italy)

Supporting information for this article is available on the WWW under https://doi.org/10.1002/cmdc.202300046

ChemMedChem

Research Article
doi.org/10.1002/cmdc.202300046

Chemistry
Europe

European Chemical
Societies Publishing

Recently, our research group developed a large library (GEBR library) of different selective PDE4D inhibitors (PDE4DIs) maintaining the catechol portion of the well-known PDE4 inhibitor Rolipram (Figure 1), featuring at the same time different substitutions in place of the lactam group of this reference compound.[16–19]

As shown in Figure 1, different series of the so-called GEBR compounds (GEBRs) have been developed, exhibiting most of them a five-membered ring as bioisostere replacement of the Rolipram lactam group, as in **GEBR-26g** and of **GEBR-32a**. Along with this, the cited **GEBR-26g**, **GEBR-32a** and the related analogues were endowed with additional terminal H-bonding groups, such as amide moieties or alkoxy groups.[18,19]

Simultaneously, structural simplification strategies have been applied leading to the more effective oxime-based GEBRs, acting as PDE4DIs, such as **GEBR-20b** (Figure 1).[16]

These synthetic efforts have been accompanied by X-ray crystallographic analyses; these data have been derived including the aforementioned GEBRs (6FDC, 6F8U and 6F8X PDB codes),[19] as well as further analogues, as reported in Supporting Information Table S2. These experimental studies reveled the role played by: (i) the terminal basic groups of the PDE4D inhibitor and by (ii) the central linker able, when endowed with H-bonding moieties, to stabilize the inhibitor at the enzyme catalytic site, thanks to several water-bridges. In particular, **GEBR-32a** (PDB code = 6FDC) and **GEBR-20b** (PDB code = 6F8U) featuring a morpholine ring as poorly flexible basic core, interact by this basic group with Ser374, Ser521 and Gln509 (Supporting Information Figures S1 and S2). Then, both the two PDE4DIs were engaged in H-bonds with the key residue Gln535, by means of the oxygen atoms of the catechol portion.

In addition, only **GEBR-20b**, bearing a smaller linker than **GEBR-32a**, was able to efficiently occupy the PDE4D catalytic site in order to display further contacts with the biological target, such as π–π stacking with Phe538 (Supporting Information Figure S2).

Consequently, the choice of smaller polar portions as tethering moiety between the terminal basic group and the main catechol portion, proved to be the most beneficial.

As regards compound **GEBR-26g**, the introduction of a flexible terminal basic chain, enriched with H-bonding groups, (PDB code = 6F8X), allowed several water bridges and H-bonds with Asn375 (Supporting Information Figure S3). This behavior in any case guarantees the required H-bonds involving the catechol moiety and the conserved Gln535.

Herein, in order to gain some hints for the rational design of further new GEBR analogues, we deemed interesting to better

explore the putative docking mode of further chemotypes recently described in the literature, featuring PDE4 inhibitor ability. We referred to naphthyridinone-(NAP)[10] and to naphthyridine (Toddacoumalone derivatives TCD) series,[20] which were endowed with PDE4 inhibitor ability both towards the PDE4B and PDE4D isoforms, conceivably turning in very effective anti-inflammatory agents.

Thus, these series of ligands have explored by means of structure-based studies and pharmacophore modeling. In particular, molecular docking calculations of rigid and sterically hindered PDE4Is such as NAPs and TCDs offered the possibility to better explore the main key contacts featured by the ligand at the enzyme catalytic site. Performing pharmacophore modeling allowed us to derive useful guidelines for the following rational design of a new series of GEBR analogues.

Thus, a small new library of compounds (**1–3**) has been designed and preliminary evaluated in silico via molecular docking studies and pharmacokinetic (PK) properties prediction. The most promising of them have been synthesized with the aim at increasing the enzyme-ligand interactions as well as at obtain more drug-like derivatives.

Additionally, their ability to interfere with the reactive oxygen species (ROS) production has been investigated in comparison with previous PDE4DIs with the aim to identify new chemo-types endowed with antioxidant/anti-inflammatory activity, probably linked to PDE4 inhibition (see the workflow of the whole study in Figure 2).

In detail, as previously demonstrated by our GEBR compounds[21] and more recently by other PDE4I,[22] PDE4 inhibition causes ROS production inhibition and increases cAMP concentration, stimulating the activity of Nrf-2, a key transcription factor that represents one of antioxidant cellular defense mechanisms (Figure 3).[22]

Based on these considerations, to verify the in vitro antioxidant activity of most promising compounds, some of them have been tested in endothelial (EAhy926) cells and in human platelets, using **GEBR-20b** as reference compound.

The obtained results for the new developed **1–3** were in good agreement with our previous data concerning the antioxidant activity exhibited by the previous PDE4Is[21,22] and similarly to **GEBR-20b**. Collectively, biological results featured
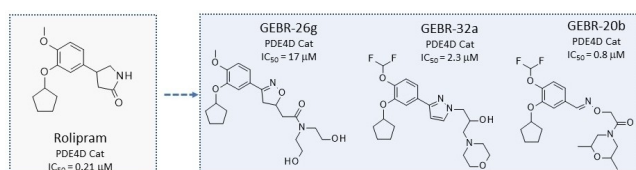
Figure 1. Chemical structure of Rolipram and PDE4DIs analogues.
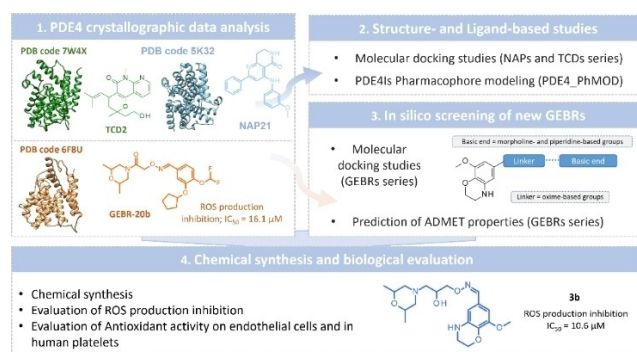
Figure 2. Workflow of the applied strategies leading to the design of novel anti-inflammatory/antioxidant agents.
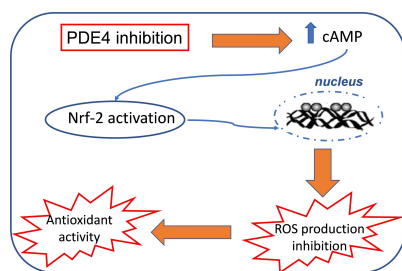
Figure 3. Effect of PDE4 inhibition on ROS production.

Figure 5. X-ray crystallographic pose of **TCD2** (C atom; green) within the PDE4D catalytic site (PDB code = 7W4X).[23] The docking pose of **TCD23a** (C atom; yellow) is also reported.

by the new synthesized compounds, closely linked to the anti-inflammatory activity and also to PDE4 inhibition, confirmed the potential application of this new chemo-type to achieve anti-inflammatory/antioxidant compounds.

Results and Discussion

Exploring in silico naphthyridine (TCDs) as PDE4 inhibitors

During the last years, several studies reported novel PDE4Is as derived from the natural compound Toddacoumalone (TC),[23] leading to the hit compound **TCD2**, as racemic mixture (see Figure 4).[20] The compound featured a naphthyridine scaffold and showed moderate potency as PDE4I, with the IC_{50} value of 400 nM. The **TCD2** bioactive conformation within the PDE4D catalytic site has been elucidated by X-ray crystallography (PDB code = 7W4X),[24] opening the possibility to proceed with the rational design of the further new analogues (see chemical structures in Supporting Information Table S3).

This allowed the inhibitor optimization as observed with the analogues **TCD23a–25a**; herein, we explored the docking mode of the novel hit-to-lead compounds **TCD23a–25a** within the PDE4 protein (PDB code = 7W4X) with the aim at deciphering the most effective key contacts in stabilizing the enzyme-inhibitor complex (the calculated docking poses in tandem with the reported scoring functions are shown in Table S4). Based on the X-ray crystallographic data, the co-crystallized inhibitor **TCD2** (PDE4D IC_{50} = 400 nM) was H-bonded to Gln369 thanks to the nitrogen atom at the position 7 of the main core, being the aromatic portion of the same ring engaged in π–π stacking with Phe372 (Figure 5). The vinyl group of TCD2 was oriented towards the hydrophobic Phe340, Met357, Ile376, Met273,
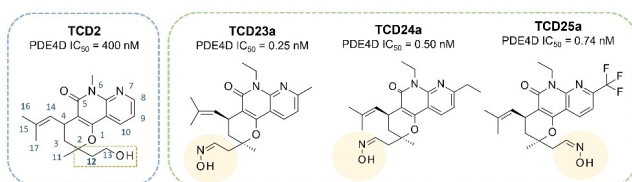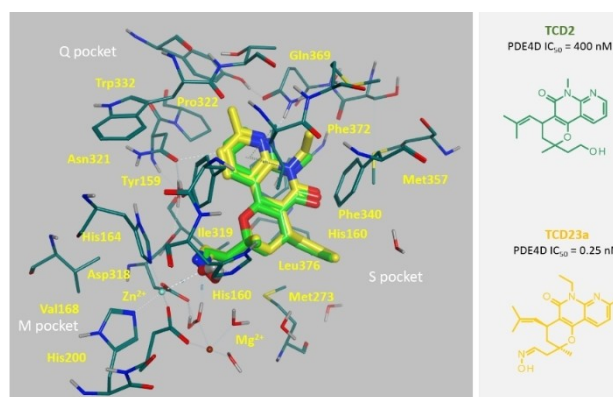
detecting Van der Waals contacts, while the terminal alkoxy substituent was projected in proximity of the two metal ions.
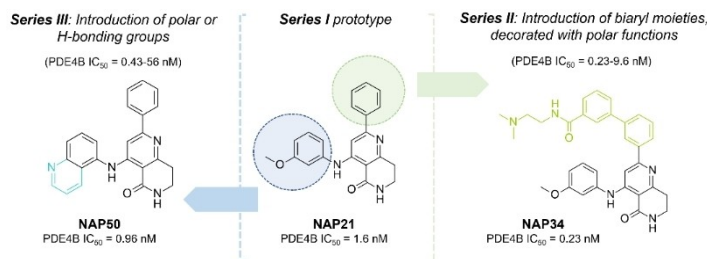
According to our calculations, the most potent **TCD23a–25a** (PDE4D IC_{50} = 0.25–0.74 nM) maintained a comparable positioning, also giving additional hydrophobic contacts with the biological target via the hydrophobic (halogenated)alkyl-based chains inserted at the tricyclic positions 6 and 8 (Figure 5). Indeed, the most effective compound **TCD23a** moved the methyl and the ethyl substituent towards Tyr329 (Q pocket) and Phe340, Met357 (S and Q pocket) respectively, whereas, the introduction of the poorly flexible and most polar oxime group, allowed **TCD23a** to better coordinate the M pocket ions and to be efficiently stabilized within the enzyme catalytic site. Notably, this kind of behavior was enlightened also by the corresponding dominant **23a** tautomer featuring the zwitterion charge onto the oxime group (Supporting Information Figure S4).

This guarantees high potency values as PDE4DIs for all the analogues **TCD23a–25a** and suggests for small substituents interacting with the narrow Q pocket, while an extended highly polar chain is required to feature water bridges and metal ion contacts.

Exploring in silico naphthyridinones (NAPs) as PDE4 inhibitors

Recent efforts reported in the literature, led to the design and discovery of a new class of potent PDE4 inhibitors, exhibiting the naphthyridinone main core (NAPs).[10] The compounds have been designed considering derivative **GSK256066** as reference compound, being in phase II clinical trials for the treatment of respiratory disorders. In addition, X-ray crystallographic data of **GSK256066** at the PDE4B2B catalytic site were available (PDB code = 3GWT).[25]

Thus, as shown in Figure 6, three series of NAPs, have been described[10] to achieve more key interactions with the solvent exposed pocket (S pocket; II series) and with the metal binding pocket (M pocket; III series), than those compounds tailored for

Figure 4. Scheme of the Toddacoumalone derivatives (TCDs) prototype TCD2 and of the further optimized analogues **TCD23a–25a**.

ChemMedChem

Research Article
doi.org/10.1002/cmdc.202300046

Chemistry
Europe
European Chemical
Societies Publishing

Figure 6. Scheme of the main chemical substitutions afforded at the NAP core towards the NAP II series and the NAP III series, with respect to the I series prototype **NAP21**. The chemical structures of **NAP34** and **NAP50**, as references for the II–III series, are also reported.

the lipophilic pocket (Q pocket; I series), such as the prototype **NAP21**.

The biological results in terms of PDE4B inhibitory ability supported the rational design process highlighting an improvement in IC_{50} values for the NAP II series (PDE4B $IC_{50} = 0.23$– 9.6 nM) and NAP III series (PDE4B $IC_{50} = 0.43$–56 nM) compounds, with respect to the first one (I series; PDE4B $IC_{50} = 1.6$– 32 nM). Chemical structures and PDE4B inhibitory ability of the herein discussed NAPs (I–III series) are reported in Supporting Information (Table S5–S6). Thus, combining the most effective substituents featured by both the previously said II and III derivatives, led to the most potent NAPs, such as **NAP74** (PDE4B $IC_{50} = 0.11$ nM), bearing the quinoline group of **NAP50** and the biaryl fragment of **NAP34** (Figure 6, Table S5–S6).

Interestingly, the X-ray crystallographic data of **NAP21** at the PDE4D catalytic site (PDB code = 5K32)[10] allow to better explore in silico the binding mode of the three NAPs series, giving some information about the main interactions which would stabilize the enzyme-inhibitor complex. On this basis, herein we proceeded with molecular docking studies of NAPs (as numbered in the previous Table S5) by means of MOE software (DOCK module)[26] exploring the most probable bioactive conformation of the most potent analogues belonging to the three I–III series, within the PDB code 5K32. The calculated binding affinity values of the predicted enzyme-inhibitor complexes are reported in Supporting Information (Table S7).

As shown in Figure S5, re-docking studies of the co-crystallized inhibitor **NAP21** (C atom, green) led to the highly comparable inhibitor docking pose (C atom; yellow), chosen as the best ranked one by the MOE scoring function (see the experimental section). On this basis, the presence of H-bonds involving the basic and the lactam nitrogen atoms of the naphthyridinone ring and the key residues Gln369 and Asn321 was confirmed, while the methoxy-phenyl substituent of **NAP21** and the unsubstituted phenyl ring were projected towards the M- and the S-pockets. This kind of positioning allowed the inhibitor to be stabilized within the enzyme catalytic site by means of water-bridges, cation-π contacts and π–π stacking with Tyr159, His160 and Phe340, Phe372, respectively. In addition, the main bicyclic core of the inhibitor was also engaged in Van der Waals contacts with Tyr159, Pro322, Tyr329 and Phe372.

The introduction of biaryl substituents, endowed with H-bonding features, led to the more potent analogues belonging to the NAP II series, which were thought to be extended towards the S-pocket (**NAP28**-**NAP35**; PDE4B $IC_{50} = 0.23$– 9.60 nM). According to our calculations, the docking positioning obtained for **NAP34** (PDE4B $IC_{50} = 0.23$ nM) guarantees the aforementioned contacts described for the prototype **NAP21**, featuring in addition further π–π stacking and water-bridges with the surrounding S-pocket water molecules thanks to the biaryl motif and the related long-chain amide substituent (Figure 7).

Applying structural variations at the previous **NAP21** aniline portion such as the introduction of amide, alkoxy and carboxylic acid at the same aromatic ring or its replacement with other heterocycles (pyridine and quinolone) allowed to derive the NAP III series (**NAP38**–**NAP64**; PDE4B $IC_{50} = 0.43$–56 nM), enriched with polar contacts with the enzyme M-pocket. Accordingly, **NAP50** (PDE4B $IC_{50} = 0.96$ nM), maintained H-bonds with the previously discussed Asn321 and Gln369, featuring further cation-π and Van der Waals contacts between the quinoline ring and His160, Met273, respectively (Figure 8).

Based on this structure-activity information, the third series of NAPs was designed, leading to the most potent analogues **NAP66**–**NAP74** (PDE4B $IC_{50} = 0.045$–1.2 nM). As shown in Figure 9, **NAP74** (PDE4B $IC_{50} = 0.11$ nM) exhibited at the same time
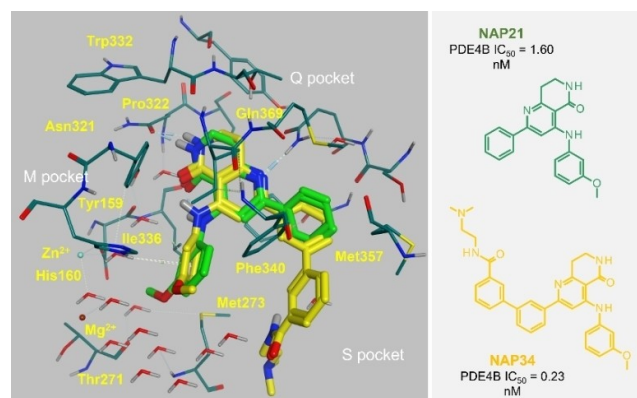
Figure 7. X-ray crystallographic pose of **NAP21** (C atom; green) within the PDE4D catalytic site (PDB code = 5K32).[10] The docking pose of **NAP34** (C atom; yellow) as representative of the NAP II series is also reported.
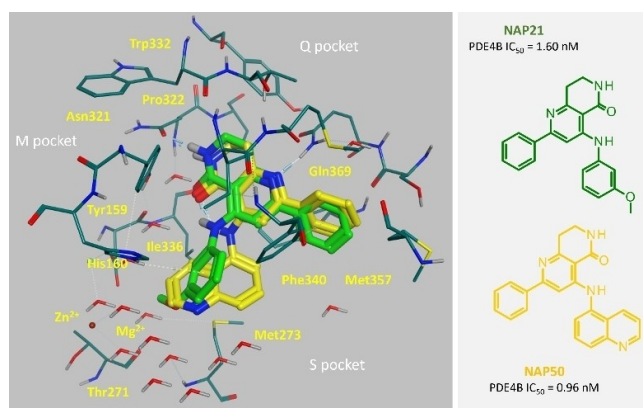
Figure 8. X-ray crystallographic pose of **NAP21** (C atom; green) within the PDE4D catalytic site (PDB code = 5K32).[10] The docking pose of **NAP50** (C atom; yellow) as representative of the NAP III series is also reported.
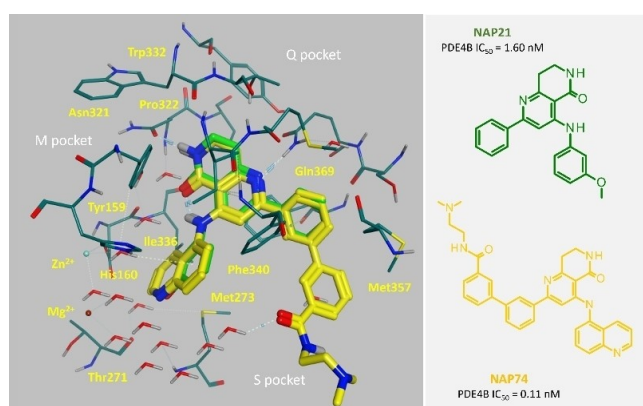
Figure 9. X-ray crystallographic pose of **NAP21** (C atom; green) within the PDE4D catalytic site (PDB code = 5K32).[10] The docking pose of **NAP74** (C atom; yellow) as optimized NAP analogues as PDE4 inhibitor is also reported.

all the optimized contacts previously discussed for the analogues **NAP34** (with the enzyme S-pocket) and **NAP50** (with the enzyme M-pocket), being one of the most potent PDE4I within all the NAP series.

The development of different series of NAPs (I–III) strongly supported the design of novel compounds better stabilized within the enzyme catalytic site thanks to a bulky bicyclic core interacting especially with the Q pocket.

Pharmacophore modeling of PDE4Is

The development of different series of NAPs (I–III), allowed us to proceed with the search of a PDE4 pharmacophore model (PDE4_PhMOD) derived thanks to the pharmacophore search tool implemented in MOE software, which works in order to identify the most recurrent pharmacophore moieties featured by the collected pool of PDE4Is. Any pharmacophore feature is classified by an identification code (ID), in tandem with the percentage by which this moiety is shared by all the set

compounds (SCORE), by a radius representing the maximum space within this pharmacophore features can be placed with respect to the inhibitor (RADIUS), and by a symbol explaining the interaction with the enzyme (EXPRESSION).

In particular, in order to investigate the specific requirements supporting the design of new promising compounds, featuring PDE4 inhibitory ability, we focused on those NAPs endowed with high potency values (PDE4B IC_{50} values < 1.60 M). This threshold was chosen in order to guarantee the structural features turning into inhibitors whose potency would be higher than that of the prototype **NAP21** (PDE4B IC_{50} = 1.60 nM).

About fifteen compounds over the collected forty-three analogues fulfilled the previously described feature, as listed in Table S8. On this basis, the best ranked docking conformers of these fifteen NAPs (IC_{50} values < 1.60 nM), were retained in order to develop the following pharmacophore analysis (see the experimental section).

Notably, according to these data, NAPs belonging to the second and third series represent about the 20% and the 13% of the collected most potent NAPs, while combined analogues covered about the 67% of the PDE4Is featuring higher potency than the prototype **NAP21**. This piece of information confirmed once again the effective role played by a proper choice of substituents to interact with the M and S pocket, towards more potent derivatives.
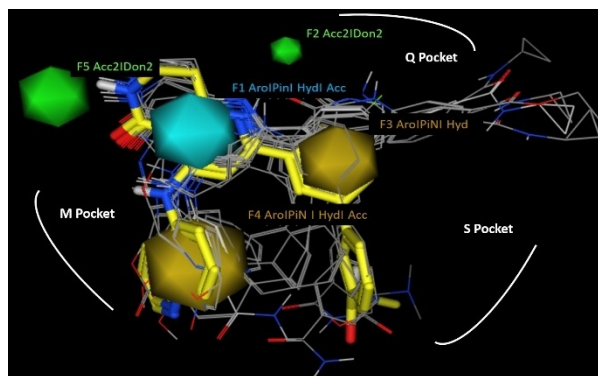
Docking-based alignment of derivatives is shown in Figure 9, being compound **NAP74** (in yellow) as one of the most potent optimized naphthyridinones herein analyzed for the search of the PDE4_PhMOD.

As listed in Table 1, at least 70% of the reported NAPs shared five pharmacophore moieties conceivably involved in the PDE4 inhibitor activity, suggesting for bulky and/or aromatic groups tethered to a main heterocyclic core, properly enriched with H-bonding pendants.

As shown in Figure 10, the developed model highlights the role played by a common heterocyclic core enriched with H-bond acceptor groups (namely F1:Aro|PiN|Hyd|Acc), as the naphthyridinone ring (see Figure S6). This should be properly tethered to further bulky (hetero)aromatic rings (namely F3: Aro|PiN|Hyd) and to bulky (aromatic or aliphatic groups) exhibiting H-bonding functions (namely F4:Aro|PiN|Hyd|Acc). Accordingly, the potent analogue **NAP74** experienced a phenyl and a quinolone ring at the corresponding F3:Aro|PiN|Hyd and F4:Aro|PiN|Hyd|Acc polyhedral (Figure 9).

Table 1. Recurrent pharmacophore features shared by 70% of the PDE inhibitors, featuring the NAP core herein explored, and related ID, score, radius, and expression values.

ID	Score [%]	Radius [Å]	Expression
F1	100	3.81	Aro|PiN|Hyd|Acc
F2	87	1.42	Acc2|Don2
F3	87	2.36	Aro|PiN|Hyd
F4	87	2.89	Aro|PiN|Hyd|Acc
F5	73	2.18	Acc2|Don2

ChemMedChem

Research Article
doi.org/10.1002/cmdc.202300046

Chemistry
Europe
European Chemical
Societies Publishing

Figure 10. Pharmacophore model of the most potent NAPs previously reported in Table S8. Alignment of the fifteen derivatives is shown, being **NAP74**.shown in stick and taken as reference compound (C atom; yellow).

H-bonding functions are named as F Don and F Acc. Aliphatic or Aromatic lipophilic groups are labelled as F Aro|Hyd.

In addition, the main heterocyclic ring should be decorated with H-bonding features, as suggested by F2:Acc2|Don2 and F5:Acc2|Don2.

Notably, the reciprocal distances as calculated between all the previously cited F1-F5 features (Supporting Information Figure S6) represent a useful tool for the further design not only of NAP analogues, but also of novel PDE4Is, even if based on different chemotypes.

In particular, the H-bonding groups exemplified by F2:Acc2|Don2 and F5:Acc2|Don2 should be at 4.68 Å and 5.28 Å from the heterocyclic core, reported as F1:Aro|PiN|Hyd|Acc, which would be placed at 5.35 Å and at 5.42 Å from the pendants F3:Aro|PiN|Hyd and F4:Aro|PiN|Hyd|Acc. These two features should be at 6.72 Å to each other, giving a new perspective for the design of further chemo-types in place of the phenyl and quinoline rings, being also at 4.71 Å and at 8.49 Å far from F2:Acc2|Don2 and F5:Acc2|Don2, respectively.

As a result, these data revealed the relevance of branched chemotypes, such as the naphthyridinone ring, as tethered to H-bonding groups and hydrophobic substituents (such as the quinoline and long-chain-amide of **NAP74**), in order to be efficiently stabilized at the three Q-, M- and S-pockets. Indeed, the presence of polar groups resulted to be highly required to guarantee metal-ligand interactions and water-bridges contacts with the M and S pockets, being in agreement with the crystallographic studies previously cited.

Design of novel GEBR analogues 1–3

The results obtained by the previous data about the pharmacophore features exhibited by NAPs, as well as the main contacts involved in the NAP- or TCD- PDE4 complexes, allowed us to qualitatively evaluate new series of putative PDE4Is. To pursue further information to guide the design and chemical synthesis of novel GEBR analogues, herein we explored the X-ray

crystallographic data of our previous **GEBR-32a**, **GEBR-26g** and **GEBR-20b** as PDE4Is,[16,17] in comparison with those of **NAP21**[10] and of **TCD2**.[20]

Initially, we explored the putative protein flexibility because of the cited GEBR binding, by superimposition the 6FDC, 6F8U and 6F8X PDB codes.

The corresponding RMSD values calculated with respect to the alpha carbon atoms (CA atoms), revealed low structural differences spanning from 0.20 Å to 0.31 Å, thus supporting for minimal discrepancies among the explored experimental data (Supporting Information Figure S7). In detail, the alignment and superimposition of all the aforementioned three PDB codes led to an overall RMSD value of 0.244 Å.

Interestingly, the use of all the atoms to calculate the superposition, thus including evaluation of sidechain symmetries, led to an overall adequate RMSD value (overall RMSD = 0.494 Å) within the recommended limit of 2 Å, as reported in Supporting Information Figure S7.

In particular, despite of the aforementioned discussed positioning of the specific co-crystallized inhibitors (see the previous Figures S1–S3), the 6F8X (RMSD = 0.42 Å) was the most structurally similar to 6FDC. However, it should be noticed that the main flexible portion of the PDE4D protein involves a number of the first fifty amino acids, corresponding to the PDE4D 256–298 residues, and not those involved in the inhibitor binding.
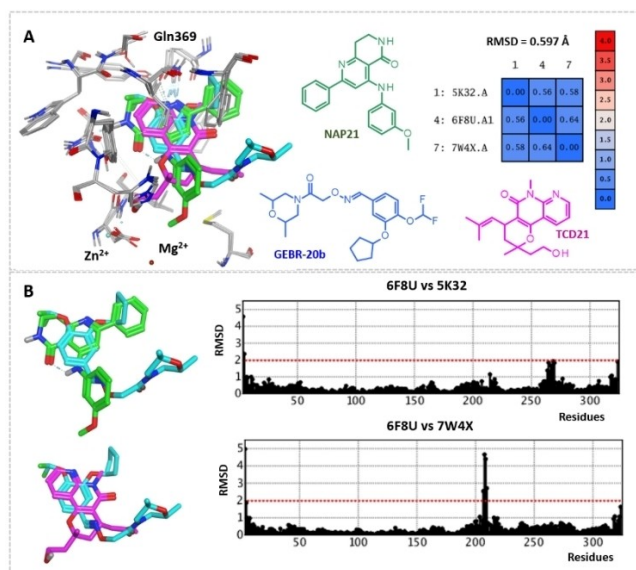
Then, we compared and superposed the 6F8U PDB code (involving **GEBR-20b**), taken as representative of the most GEBR so far derived, with the experimental data concerning the NAP (PDB code = 5K32) and TCD (PDB code = 7W4X) series. This comparison highlighted pairwise percentage residue identity values higher than 98.8% to each other.

The use of all the atoms to calculate the superposition led to an overall acceptable RMSD values (overall RMSD = 0.597 Å), as shown in Figure 11A. In particular, the main flexible portion of the PDE4D and PDE4B proteins involves several residues not involved in the inhibitor binding, as previously reported (Figure 11B).

By superimposition of the 6F8U with 5K32 and 7W4X PDB codes, new hints for the design of novel putative PDE4Is could be derived, highlighting the effectiveness of the catechol portion of the in-house inhibitors as bioisostere replacement of the NAP(TCD) series naphthyridinone(naphthyridine) ring. As shown in Figure 11A, the NAP21 bicyclic core guarantees the required key contacts with the conserved glutamine residue (Gln369 in the 5K32 PDB code), being able to mimic the positioning of the oxygen atom of the **GEBR-20b** catechol portion, as well as by the naphthyridine ring of **TCD2**.

While the **GEBR-20b** oxime-based group was projected towards the metal pocket, the alkoxy function of **TCD2** and the m-methoxy phenyl ring of **NAP21** were oriented in the proximity of the same metal ions.

On this basis, a novel series of stiffened catechol-based derivatives **1–3** has been designed (Table 2). In analogy with the same GEBR prototype, an oxime-based function tethering with the terminal morpholine-based or piperidine basic chain has been maintained.

ChemMedChem

Research Article
doi.org/10.1002/cmdc.202300046

Chemistry
Europe
European Chemical
Societies Publishing

Figure 11. Superimposition of the 5K32, 6F8U and 7W4X PDB codes in presence of **NAP21**, **GEBR-20b** and **TCD2**, respectively. The corresponding RMSD values and the chemical structure of the inhibitors are also reported (A). A comparison of the crystallized bioactive conformation of **GEBR-20b** (in cyan) with that of **NAP21** (in green) and **TCD2** (in magenta) is reported, in presence of the related protein-protein RMSD plot (B).

Table 2. Chemical structure of new projected compounds **1–3**.

Compd	Linker	Terminal end
1a	CH_2CO	
1b	CH_2CO	
1c	CH_2CO	
2a	CH_2CH_2CO	
2b	CH_2CH_2CO	
3a	$CH_2CH(OH)CH_2$	
3b	$CH_2CH(OH)CH_2$	
3c	$CH_2CH(OH)CH_2$	

All these structural variations are expected to fulfil the previously cited suggestions in terms of occupancy of the catalytic site and interactions with most of the known key residues supporting the PDE4D inhibitory activity. Indeed, this choice is thought to guarantee additional contacts with the surrounding residues, such as the previously mentioned

Phe538. Along with this, we also considered to better exploit structural variation at the catechol group, which proved to be quite anchored within the enzyme cavity delimited by hydrophobic and aromatic residues, such as Tyr325, Trp498 and Met503, in order to gain further contacts especially with the flat aromatic residues Phe506 and Phe538.

Notably, this kind of structural variation results qualitatively in good agreement with the information previously described by the PDE4_PhMOD. Indeed, the newly designed **2b** partially fulfilled the requirements described by F1:Aro│PiN│Hyd│Acc thanks to the stiffened catechol-based core, which also guarantees the proper H-bonding functions in proximity of F2:Acc2│Don2 and F5:Acc2│Don2, by the oxygen atoms and the nitrogen atom of the main scaffold (see Figure S8). In addition, the oxime-based spacer and the terminal morpholine ring of **2b** moved near the F4:Aro│PiN│Hyd│Acc and to the long/chain amide portion of **NAP74**, suggesting for a quite longer linker as experienced by **3b** as optimal spacer to simulate the positioning exhibited by the previous **NAP74**. On the other hand, the methoxy group of the newly designed compounds **1–3** would be modified in bulkier substituents with lipophilic properties, in order to better fulfill the requirements represented by F3:Aro│PiN│Hyd.

In silico screening of compounds 1–3 as putative PDE4Is

Taking into account the previously discussed X-Ray data of **GEBR-32a**, **GEBR-20b** and **GEBR-26g**, we evaluated in silico the putative PDE4 inhibitory ability of the novel **1–3** compounds via molecular docking studies. Initially, we applied re-cross docking of the 6FDC, 6F8U and 6F8X co-crystallized inhibitors and then molecular docking calculation on **1–3**. Indeed, deepening re-cross docking simulations are exploited to evaluate the most adequate docking protocol to be applied for simulate the experimental data, following a procedure already applied in the literature.[27] Herein, the three series of re-cross docking calculations were performed by means of MOE software, Dock module.[26]

The top five best scored docking positioning for **GEBR-32a**, **GEBR-20b** and **GEBR-26g** as PDE4DIs docked within the aforementioned three different PDB codes are listed in Tables S9–11, suggesting for comparable protein-ligand complexes. For each series of inhibitor with respect to the three crystallized proteins, the predicted ΔG values were around −8 to −6 kJ/mol.

In addition, MOE Dock module was able to suggest similar docking poses if compared to the related X-ray crystallographic data, featuring RMSD values spanning from 1.172 Å to 2.134 Å (Figure 12).

On this basis, taking into account: (i) the low RMSD value observed in the case of re-cross docking done on 6F8U and (ii) the structural similarity of the central linker featured by **GEBR-20b**, the following molecular docking studies about the aforementioned compounds **1–3** were developed thanks to the 6F8U PDB code, by MOE Dock (the scoring functions related to
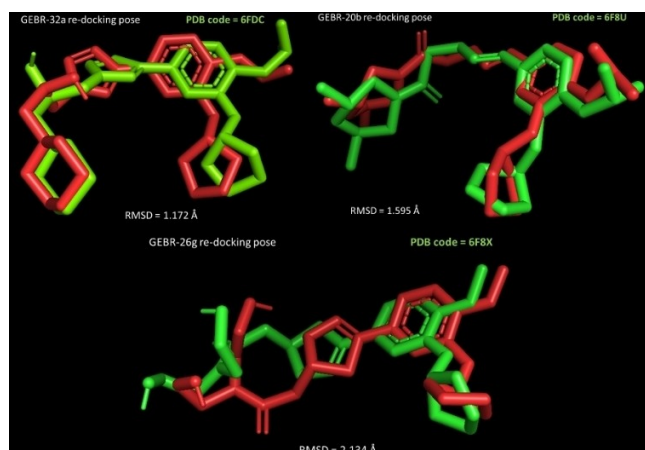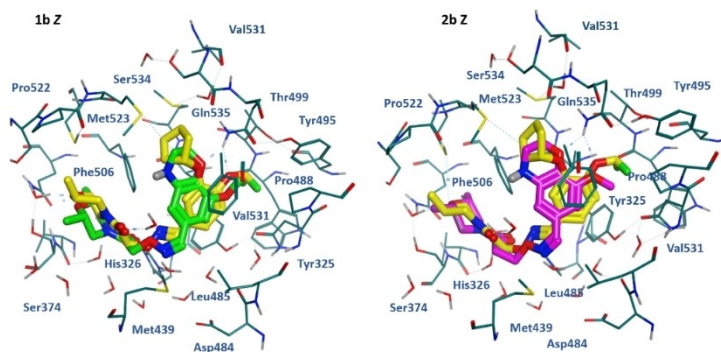
Figure 12. Comparison of the best scored GEBR docking poses (red ligand) with respect to the same crystallized compound at the 6FDC, 6F8U and 6F8X PDB codes (green ligand) by MOE Dock calculation. RMSD values have been evaluated by PyMOL.[28]

these compounds are listed in Supporting Information Table S11).

According to our results, the morpholine-based terminal chain was preferred to the piperidine one, being particularly effective when accompanied by the extended alkyl amide
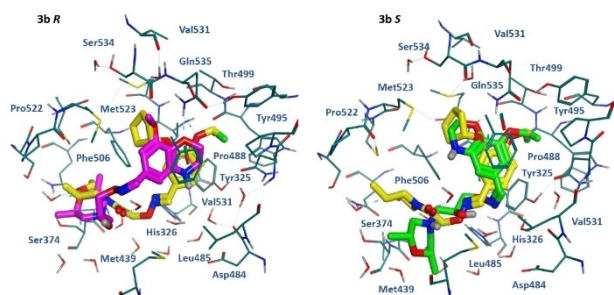
Figure 13. Docking mode of the newly designed **3 b** *R* (left) and *S* enantiomers (right) within the 6F8U PDB code. The two derivatives are reported in magenta and green, respectively, in presence of the co-crystallized **GEBR-20 b** (C atom; yellow).

groups or by the alkoxy spacer, such as featured by the compounds **2** and **3**, respectively. As shown in Figure 13, the 2,6-dimethylmorpholine group of **3 b** (*R* and *S* enantiomers) properly overlapped the corresponding group of the **GEBR-20 b** reference compounds, as well as the corresponding oxime portion, especially in the case of the S enantiomer.
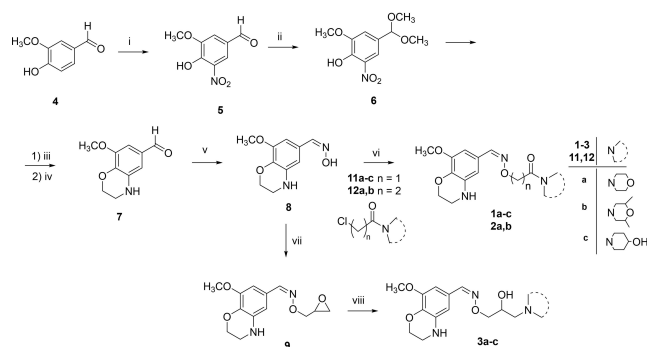
As regard the amide-containing analogues **1 b** and **2 b**, both maintained the same positioning if compared to the crystallized **GEBR-20 b**, being both properly folded thanks to the alkyl amide chain. Therefore, the two novel compounds experienced comparable docking modes as shown in Figure 14, being the *Z* isomers predicted as the most favorable.

Chemistry

Compounds **1**–**3** were synthesized as reported in Scheme 1.

In detail, 4-hydroxy-3-methoxybenzaldehyde (vanillin) **4** was transformed in 4-hydroxy-3-methoxy-5-nitrobenzaldehyde **5** following literature procedure.[29] Before the reduction of the nitro group, protection of the aldehyde group is necessary. Thus, aldehyde **5** was transformed into corresponding acetal **6** by heating in methanol at reflux for 2 hours under nitrogen atmosphere;[30] then compound **6** was immediately subjected to reduction, using the H-cube hydrogenator (Method A) at room temperature and atmospheric pressure, flow of 1 mL/min, using a 10% Pd/C as catalyst. The same reaction could be performed using hydrazine monohydrate in methanol at 70–75 °C for 40 minutes (Method B). During the reduction, a deprotection of the aldehyde function also occurred; consequently, the crude was quickly treated with 1,2-dibromoethane to give 3,4-dihydro-2*H*-8-methoxy-1,4-benzoxazin-7-carbaldehyde **7**. The latter was reacted with hydroxylamine hydrochloride in a mixture of water/ethanol at 60–70 °C for 4 hours to easily obtain the desired oxime **8**. Although formation of *E/Z* mixtures is possible, only *Z* isomer of oxime **8** has been always obtained, as confirmed by ^{1}H- and ^{13}C-NMR spectra in accordance with literature data.[31] This attribution was possible based on the [1]H-chemical shift of the signal of the C(H)=N group which appeared at 7.99 ppm as a singlet (see Figure S9).

Figure 14. Docking mode of the newly designed **1 b** *Z* isomer (left) and **2 b** *Z* isomer (right) within the 6F8U PDB code. The two derivatives are reported in green and magenta respectively, in presence of the co-crystallized **GEBR-20 b** (C atom; yellow).

ChemMedChem

Research Article
doi.org/10.1002/cmdc.202300046

Chemistry Europe
European Chemical
Societies Publishing

Scheme 1. Synthesis of new compounds **1–3**. Reagents and conditions: (i) acetic acid, HNO₃ 60%, r.t., 30 min, 84%;[29] (ii) an. MeOH, 60–70 °C, 8 h, 100%;[30] (iii) Method A: H-cube, full H2 mode, Pd/C 10%. Method B: hydrazine monohydrate, MeOH, 70–75 °C, 40 min (yields not calculated); (iv) an. DMF, K₂CO₃, 1,2-dibromoethane, 60–70 °C, 18 h, 74%; (v) hydroxylamine hydrochloride, EtOH 95%, H₂O, 60–70 °C, 4 h, 43%; (vi) 1) an. DMF, K₂CO₃, r.t., 10–20 min.; 2) chloroacetyl or chloropropionyl amides **11a–c** or **12a,b**,[32] 50–70 °C, 8 h, 25–94%; (vii) epichlorohydrin, EtONa, an. DMF, 40–50 °C, 18 h, 41%; (viii) excess of morpholine or 2,6-dimethylmorpholine (for **3a** and **3b**) or piperdin-4-ol (for **3c**), an. DMF, 50–70 °C, 18 h, 26–30%.

The desired compounds **1a–c** and **2a,b** were obtained by the reaction of the oxime **8** with the suitable chloro-amides **11a–c** and **12a,b**, synthesized by us following literature method,[32] whereas reaction of oxime **8** with sodium ethoxide and epichlorohydrin in an. DMF at 40–50° C for 18 hours gave intermediate **9**; finally, derivatives **3a–c** were obtained by reaction of oxirane **9** with an excess of morpholine (**3a**), 2,6-dimethylmorpholine (**3b**) or with piperdin-4-ol (**3c**) in an. DMF.

Biological evaluation of new compounds 1–3 as anti-inflammatory/antioxidant agents

To preliminarily evaluate biological activity of new synthesized compounds, we select compounds **1b** and **3b**, predicted as the most active (see Figure 13 and 14) and showing the same amino terminal group but a different chain linker, to investigate their ability to interfere with ROS production in comparison with previous PDE4DI **GEBR-20b**, used as reference compound.

It is in fact known that ROS, as H₂O₂ and HOCl, provoke a damage of inflamed tissue and enhance the inflammatory response by their synergic proinflammatory activities; consequently, inflammation and oxidative stress are strictly related, since inflammation can lead to ROS production, causing tissue damage in different pathologies as neurodegeneration,[33] aging,[34] inflammatory diseases[35,36] and cerebral ischemia.[22,37] In addition, as reported before (Figure 3), PDE4Is, enhancing intracellular cAMP levels, exert inflammatory activity and ROS production inhibition,[22,38,39] as already observed for different PDE4Is.[21,22,36] For these reasons, selected compounds **1b** and **3b** were tested as ROS production inhibitors in different cellular behaviors, as endothelial cells and human platelets.

In endothelial cells, the antioxidant activity of the selected compounds was evaluated using H₂O₂ as pro-oxidizing agent.[40] Results reported in Figure 15 evidence that in endothelial cells,
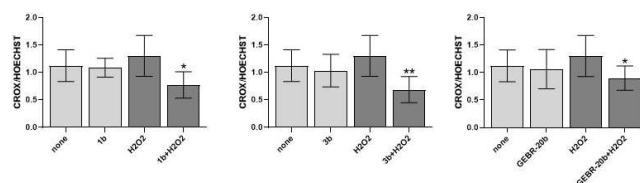
Figure 15. ROS production inhibition in endothelial EAhy926 cells. Bar graph of the ROS assay evaluated as CellROX to Hoechst fluorescence ratio on endothelial cells pre-treated with compounds **1b**, **3b** and **GEBR-20b** at 10 μM and treated with 50 μM H₂O₂. Unpaired student's t-test: *$p < 0.05$ and **$p < 0.005$ vs H₂O₂.

1b, **3b** and reference compound **GEBR-20b** show similar significative antioxidant effect, being able to inhibit the H₂O₂-induced ROS level increase. Collectively the three selected compounds have similar antioxidant capacity, since they show IC₅₀ values in the same range: 12.3, 10.6 and 16.1 μM for **1b**, **3b** and **GEBR-20b** respectively (Table 3).

Conversely in human platelets, in which ROS levels were quantified by the oxidation of 2',7'-dichlorofluorescein (DCFH), the selected compounds exert just a light antioxidant effect, since the obtained IC₅₀ values are 274, 310 and 280 μM for **1b**, **3b** and **GEBR-20b** respectively, almost 30 times higher than that observed in endothelial cells (Table 3).

Collectively these biological data, especially in endothelial cells, confirm that new projected derivatives **1–3** block ROS production and exert antioxidant properties similarly to well-known PDE4I **GEBR-20b** representing a good starting point for the development of new chemo-types with antioxidant/anti-inflammatory properties.

In silico prediction of ADMET properties

As deeply reported in the literature,[41,42] the process of drug discovery takes advantage of the absorption, distribution, metabolism, excretion properties (ADME) in silico prediction. In the search of novel and drug-like compounds featuring anti-inflammatory behavior, herein we evaluated in silico pharmaco-kinetic and toxicity properties (ADMET parameters) of compounds **1–3**. The results have been compared with those calculated for reference compounds of the TCD and NAP series. Furthermore, prediction of the same properties for the known PDE4Is Rolipram and Apremilast has been considered.

Table 3. Inhibitory effect of previous compounds **1b**, **3b** and **GEBR-20b** (used as reference compound) on ROS production in endothelial cells (EAhy926) and in human platelet expressed as IC₅₀ (μM) values.

|	ROS production inhibition IC₅₀ [μM][a]	
	Endothelial cells (EAhy926)	Human platelets
1b	12.3 ± 0.2	274 ± 27
3b	10.6 ± 0.2	310 ± 44
GEBR-20b	16.1 ± 0.2	280 ± 22
[a] Reported data are the mean ± SD obtained in at least three (for endothelial cells) and five (for human platelets) different experiments each performed in duplicate.		

Initially, we considered explored putative violation of the well-known Veber's rule[43] and Lipinski's rule,[44] in terms of prediction for logarithmic ratio of the octanol-water partitioning coefficient (cLogP), the molecular weight (MW) of compounds, for the related H-bonding acceptor number (HBA), or donor groups (HBD), and for the number of rotatable bonds (nRot_bond). The derivatives topological polar surface area (TPSA) and putative oral bioavailability as a percentage (F%) have been also calculated (Table 4).

Based on the Lipinski's rule, drug-like compounds exhibit MW < 500, cLogP < 5, HBA < 10 and HBD < 5, while the rule reported by Veber stands for drug bioavailability as nRot_bonds ≤ 10, sum of HBA and HBD < 12 and for TPSA values ≤ 140 Å².

According to our PK parameters prediction, all the derivatives fulfil both the Lipinski's rule and the Veber's rule, with the exception of the optimized naphthyridinone **NAP74**, being the corresponding MW > 500.

All the newly described **1**–**3** featured drug-like properties and high predicted oral bioavailability percentage values, in good agreement with those of the previously developed PDE4Is **GEBR-26g**, **GEBR-32a** and **GEBR-20b**.

Successively, in silico prediction of ADMET parameters was also performed in terms of human intestinal absorption (HIA), estimation of the plasmatic protein binding event (%PPB), volume of distribution (Vd), ligand affinity toward human serum albumin (LogKa HSA), prediction of the probability of human ether-a-go-go related gene (hERG) channel inhibition at clinically relevant concentrations (Ki < 10 µM) and of endocrine system disruption events (Table 4). Notably, the newly developed **1**–**3** were endowed with lower toxicity based on (hERG)
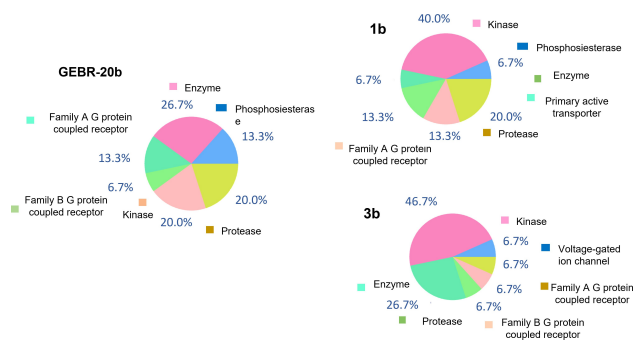
Figure 16. Prediction of putative target preferences featured by the PDE4 inhibitor **GEBR-20b** and by the new analogues **1b** and **3b**.

channel inhibition or endocrine system disruption events if compared to **NAP 74** (Table 4).

In the search of putative new hit-to-lead compounds, current in silico profiling models or website, predicting the potential compound liabilities, are nowadays deeply exploited to sustain the drug development and optimization process.[45] Herein, we supported the drug-like profile of the most interesting compounds **1b** and **3b** verifying the absence of PAINS (Pan Assay Interference structures), as estimated via SwissADME website.[46] Then, prediction of putative biological target(s) for the two analogues were performed, by means of SwissTarget,[47] as well as for the PDE4I**GEBR-20b**. As shown in Figure 16, the prototype **GEBR-20b** was predicted as PDE4-

Table 4. Calculated features as suggested by the Lipinski's rules and by the Veber's rules, referred to the novel compounds **1**–**3** (highlighted in cyan). The same prediction for the previously developed **GEBR-26g**, **GEBR-32a** and **GEBR-20b** has been reported as well as for the reference **NAP21**, **NAP74**, **TCD23a**, Rolipram and Apremilast. Reliability index values for a number of descriptors are shown as R.I. (values higher than 0.30 are ranked as reliable by the software).

Compd	LogP[a]	nRot. bond[b]	HBD[c]	HBA[d]	TPSA [Å²][e]	MW [Da][f]	% F[g]	HIA [%][h]	Vd [L/kg][i]	PPB [%][j]	LogKa HSA[k]	LogBB[l]	LogPS[m]	hERG inhib.[n]	Log RBA[o] > −3
1a	1.59	7	2	8	84.78	351.4	99.6	100	1.7	51	2.96	0.13	−2.4	0.28	0.03
1b	2.06	7	2	8	84.78	379.45	99.7	100	2.0	64	3.06	0.20	−2.2	0.30	0.06
1c	1.66	7	3	8	95.78	365.42	88.7	98	2.1	54	2.97	0.10	−3.0	0.12	0.02
2a	1.6	5	1	8	81.62	335.36	99.6	100	1.3	64	3.49	0.00	−2.1	0.27	0.09
2b	2.09	5	1	8	81.62	363.41	99.7	100	1.5	65	3.61	0.20	−1.9	0.30	0.10
3a	1.85	6	1	8	81.62	349.38	99.7	100	1.3	61	3.63	0.14	−2.0	0.22	0.07
3b	2.35	6	1	8	81.62	377.43	99.6	100	1.5	68	3.76	0.29	−1.8	0.30	0.09
GEBR-26g	1.17	10	2	8	100.82	406.47	99.6	100	1.4	66	3.37	−0.16	−2.5	0.27	0.03
GEBR-32a	2.08	9	1	7	68.98	437.48	99.6	100	2.2	84	4.2	−0.15	−1.9	0.89	0.09
GEBR-20b	2.77	8	0	7	69.59	426.45	99.4	100	2.1	77	3.82	0.37	−1.4	0.70	0.10
TCD23a	3.66	4	1	6	75.02	369.46	84.8	100	2.6	92	4.32	−1.30	0.4	0.31	0.23
NAP21	3.72	4	2	5	63.25	345.39	90.8	100	3.5	98	5.25	−0.32	−1.3	0.16	0.64
NAP74	4.32	8	3	8	99.25	556.66	99	100	7.1	99	5.7	−2.00	−0.4	0.75	0.56
Rolipram	1.87	4	1	4	47.56	275.34	99.6	100	1.4	63	3.69	0.13	−1.6	0.08	0.05
Apremilast	1.7	8	1	9	127.46	460.50	39.9	100	0.99	90	4.27	−0.53	−2.2	0.18	0.00

[a] Logarithmic ratio of the octanol–water partitioning coefficient. [b] Number of rotatable bonds. [c] Number of H-bond donors. [d] Number of H-bond acceptors. [e] Topological polar surface area. [f] Molecular weight. [g] Percentage oral bioavailability. [h] Human intestinal absorption: percentage of the molecule able to pass through the intestinal membrane. [i] Predicted volume of distribution of the compound in the body. [j] Plasma protein binding. [k] Ligand affinity toward human serum albumin (R.I. > 0.3). [l] Extent of brain penetration based on ratio of total drug concentrations in tissue and plasma at steady-state conditions. [m] Rate of brain penetration; PS: permeability-surface area product, derived from the kinetic equation of capillary transport. [n] Probability of human ether-á-go-go-related gene (hERG) channel inhibition at clinically relevant concentrations (K_i < 10 µM; R.I. > 0.4). [o] Estrogen receptor disruption (R.I. > 0.4); RBA represents the relative binding affinity with respect to that of estradiol. Compounds showing LogRBA > 0 are classified as strong estrogen binders, while those showing LogRBA < −3 are considered non-binders.

targeting ligand, being in any case prone to interact with enzyme families (such as protease, general enzymes or kinases).

Similarly, **1b** and **3b** were predicted as enzyme binders, in particular towards kinases and proteases, being **1b** also reported as PDE4 ligand. It should be noticed that the known PDE4Isexplored as clinical candidates Apremilast and Rolipram were also reported as kinase and phosphodiesterase ligands (Supporting Information Figure S24).

Conclusion

Obtained results suggested that new designed compounds **1–3**, as hypothesized by molecular docking simulations, could represent a new chemical entity, characterized by a modified catechol group, able to gain further contacts especially with the flat aromatic residues of Phe506 and Phe538 of PDE4 enzyme, as new GEBR compounds recently reported.[48] Indeed, the structural variations of new obtained compounds are expected to better fit the catalytic site and to interact with the key residues, supporting the PDE4D inhibitory activity.

Regarding biological activity, the most active predicted compounds **1b** and **3b** exert antioxidant activity, particularly in endothelial cells. In fact, **1b** and **3b** block ROS production with IC_{50} values about 10 μM, comparable to reference compound **GEBR-20b** and similarly to previous GEBRs and other PDEIs recently reported,[21,22] whereas in platelet tested derivatives show lower antioxidant activity (IC_{50} about 200 μM). On the other hand, ROS production inhibition in different behaviors confirmed the pharmacological properties, closely linked to anti-inflammatory action and PDE4 inhibition, of these new derivatives and the potential application of this new chemotype to achieve new drug-like compounds.

Experimental Section

General information

Chiminord and Aldrich Chemical (Milan, Italy) purchased all chemicals. Solvents were reagent grade. All commercial reagents were used without further purification. Aluminium backed silica gel plates (Merck DC-Alufolien Kieselgel 60 F254, Darmstad, Germany), were used in thin-layer chromatography (TLC) for routine monitoring the reaction course. Detection of spots was made by UV light. Merck Silica gel, 230–400 mesh, was used for chromatography. Flash chromatography was performed using Isolera one instrument (Biotage, Uppsala, Sweden) using Silicagel column. Melting points are not "corrected" and were measured with a Büchi M-560 instrument (Büchi instruments, Flawil, Switzerland). IR spectra were recorded with a Perkin- Elmer 398 spectrophotometer (Perkin-Elmer, Milan, Italy). 1H NMR spectra were preliminary recorded on a Varian Gemini 200 (200 MHz, Varian Gemini, Palo Alto, CA, USA), then and 1H and 13 C NMR were acquired on a Jeol 400 MHz spectrometer (JEOL USA, Inc., Peabody, MA, USA) at 400 and 101 MHz, respectively. Fully decoupled 13 C NMR spectra were reported. Chemical shifts are reported as δ (ppm) relative to tetramethyl silane (TMS) as internal standard; signals were characterized as s (singlet), d (doublet), t (triplet), q (quartet), m (multiplet), br s (broad signal); J in Hz. IR spectra were recorded

with a Perkin- Elmer 398 spectrophotometer (Perkin-Elmer, Milan, Italy). Elemental analysis was determined with an elemental analyser EA 1110 (Fison-Instruments, Milan, Italy); the purity of all synthesized compounds was > 95%; products are considered pure when the difference between calculated and found values is ± than 0.4 (Supporting Information, Table S13).

Synthesis

Synthesis of 4-hydroxy-3-methoxy-5-nitrobenzaldehyde **5**. To a solution of 4-hydroxy-3-methoxybenzaldehyde **4** (7.7 g, 50 mmol) in glacial acetic acid (80 mL) 60% nitric acid (4 mL) is slowly added at 0 °C. The reaction mixture is then stirred at room temperature for 30 minutes and then poured into ice H_2O (100 mL). A yellow solid precipitate is filtered and washed several times with H_2O. Molecular formula: $C_8H_7NO_5$. Yield: 84% [lit 70%]. M.p.: 175–177.5 °C [lit 175–177 °C][29] 1H-NMR (200 MHz, CDCl$_3$): δ 4.05 (s, 3H, OCH$_3$), 7.67 (s, 1H Ar), 8.26 (s, 1H, Ar), 9.92 (1, 1H, OH), 11.29 (s, 1H, CHO).

Synthesis of 4-(dimethoxymethyl)-2-methoxy-7-nitrophenol **6**. 4-Hydroxy-3-methoxy-5-nitrobenzaldehyde **5** (1 g, 5 mmol) is solved in an. methanol (50 mL) and heated at reflux for 2 hours under nitrogen atmosphere. The resulting solution is stored under nitrogen atmosphere and used without further purification. Molecular formula: $C_{10}H_{13}NO_7$. Yield: 100%.[30]

Synthesis of 3,4-dihydro-2H-8-methoxy-1,4-benzoxazin-6-carbaldehyde **7**.

Method A. Compound **6** (2.43 g, 5 mmol) solved in anhydrous methanol (50 mL), is reduced with H-cube hydrogenator at room temperature and atmospheric pressure (full-H$_2$ mode), with a flow rate of 1 mL/min, using Pd/C 10% cartridge as catalyst. The solution collected is cooled with ice-H_2O bath and diluted with an. DMF (50 mL).

Method B. To a solution of **6** (2.43 g, 5 mmol) in anhydrous methanol (50 mL) hydrazine monohydrate (1 mL, 32 mmol) and Pd/C (300 mg) are added. The reaction mixture is heated for 40 minutes at 75 °C and then filtered.

The solution obtained following method A or B is concentrated to half volume under reduced pressure at 30 °C, then K_2CO_3 (1.7 g, 12.3 mmol), and 1,2-dibromoethane (2 mL, 23 mmol) are added; the reaction mixture is heated at 65 °C overnight.

After cooling to room temperature, the solid obtained is filtered off and the solution is concentrated under reduced pressure and the crude is solved in ethyl acetate (30 mL). The organic phase is then washed with brine (3×20 mL), dried (MgSO$_4$) and concentrated under reduced pressure. The crude is purified by Silicagel flash chromatography using diethyl ether as eluent, to obtain a yellow pure oil. Molecular formula: $C_{10}H_{11}NO_3$ (M.W. 193.20) Yield: 64%. 1H-NMR (200 MHz, CDCl$_3$): δ 3.45–3.67 (m, 2H, NHCH$_2$), 3.97 (s, 3H, OCH$_3$), 4.39–4.68 (m, 2H, OCH$_2$), 6.90–6.07 (m, 2H, Ar), 9.78 (s, 1H, CHO). 13C-NMR (101 MHz, CDCl$_3$): δ 189.5, 150.7, 137.9, 134.0, 132.0, 106.3, 104.7, 65.4, 56.4, 38.8. Elemental Analysis calculated for $C_{10}H_{11}NO_3$ (Supporting Information Table S13).

Synthesis of (Z)-3,4-dihydro-2H-8-methoxy-1,4-benzoxazin-6-carbaldehyde oxime **8**. To a solution of 3,4-dihydro-2*H*-8-methoxy-1,4-benzoxazin-6-carbaldehyde **7** (0.4 g, 2 mmol) in absolute ethanol (4.5 mL), hydroxylamine hydrochloride (0.3 g, 4.32 mmol) previously dissolved in H_2O (2.45 mL), NaHCO$_3$ (0.75 g, 7.79 mmol) are added in small-portion; finally, H_2O (7 mL) is added and the mixture is heated at 80 °C for 4 hours. After cooling to room temperature, the mixture is concentrated at reduced pressure and stored at 0 °C to obtain a yellow solid. Molecular formula: $C_{10}H_{12}N_2O_3$. Yield: 43%. M.p.: 60.1- 62 °C. 1H-NMR (400 MHz, CDCl$_3$): δ 3.45 (t, J = 4.4 Hz, 2H,

ChemMedChem

Research Article
doi.org/10.1002/cmdc.202300046

Chemistry
Europe
European Chemical
Societies Publishing

NHCH$_2$), 3.89 (s, 3H, OCH$_3$), 4.36 (t, J=4.4 Hz, 2H, OCH$_2$), 6.49 (d, J= 1.6 Hz, 1H, Ar), 6.64 (d, J=1.6 Hz, 1H, Ar), 7.99 (s, 1H, CH=N). IR (CHCl$_3$): 3412–3100 (NH+OH), 1600 (C=N) cm^{-1}.^{13}C-NMR (101 MHz, CDCl$_3$): δ 151.1, 147.2, 138.1, 132.5, 129.2, 105.1, 102.4, 65.3, 56.1, 38.8. Elemental Analysis calculated for C$_{10}$H$_{12}$N$_2$O$_3$ (Supporting Information Table S13).

Synthesis of (Z)-3,4-dihydro-2H-8-methoxy-1,4-benzoxazin-7-carbalde-hyde O-(oxiran-2-ylmethyl)oxime 9. To a solution of (Z)-3,4-dihydro-2H-8-methoxy-1,4-benzoxazin-6-carbaldehyde oxime **8** (0.83 g, 4 mmol) in absolute ethanol (2 mL) sodium ethylate, previously prepared from Na (0.1 g, 4.35 mmol) solved in absolute ethanol (8 mL), is added and the mixture is stirred at room temperature for 15 minutes. The solvent is removed under reduced pressure and the crude is solved in an. DMF (8 mL); finally, epichlorohydrin (0.75 g, 0.55 mL, 7 mmol) is added dropwise. The mixture is heated at 40–50 °C for 18 hours. After cooling to room temperature, the reaction mixture is poured into H$_2$O (50 mL), the aqueous phase is extracted with diethyl ether (3×20 mL) and the organic phases are washed with H$_2$O (3×20 mL), dried (MgSO$_4$) and concentrated under reduced pressure. The crude is purified by Silicagel flash chromatography using diethyl ether as the eluent to obtain a brown oil used without purification. Molecular formula: C$_{13}$H$_{16}$N$_2$O$_4$. Yield: 41%. ^{1}H-NMR (200 MHz, CDCl$_3$): δ 2.75–3.09 (m, 3H, OCH$_2$+ CHO epox.), 3.16–3.55 (m, 2H, CH$_2$NH), 3.90 (s, 3H, OCH$_3$), 4.18–4.53 (m, 4H, 2CH$_2$O), 6.49 (s, 1H, Ar), 6.64 (s, 1H, Ar), 7.97 (s, 1H, CH=N). ^{13}C-NMR (101 MHz, CDCl$_3$): δ 152.0, 149.0, 137.6, 133.1, 130.7, 105.7, 103.0, 74.4, 65.2, 56.5, 50.2, 44.5, 38.8. IR (CHCl$_3$): 3400 (NH), 1608 (C=N) cm^{-1}. Elemental Analysis calculated for C$_{13}$H$_{17}$N$_2$O$_4$ (Supporting Information Table S13).

General procedure for the synthesis of compounds 1a–c. To a solution of (Z)-3,4-dihydro-2H-8-methoxy-1,4-benzoxazin-6-carbaldehyde oxime **8** (1.04 g, 5 mmol) in anhydrous DMF (10 mL), K$_2$CO$_3$ (1.23 g, 8.92 mmol) is added, and the reaction mixture is stirred for 10–20 minutes at room temperature. Then, the suitable chloroacetyl amide **11a–c** (17.48 mmol)$^{[31]}$ solved in an. DMF (7 mL) is added and the mixture is heated at 50–60 °C under nitrogen atmosphere for 8 hours. After cooling to room temperature, the mixture is poured into H$_2$O (50 mL), extracted with ethyl acetate (30×30 mL); the combined organic phases are washed with brine (30×20 mL), dried (MgSO$_4$) and concentrated under reduced pressure. The crude is purified by flash chromatography, using as the eluents firstly diethyl ether, then a mixture of diethyl ether and methanol (9:1) to obtain a yellow oil.

(Z)-8-methoxy-3,4-dihydro-2H-benzo[b][1,4]oxazine-6-carbaldehyde O-(2-morpholino-2-oxoethyl) oxime 1a. Yield: 82%. ^{1}H-NMR (200 MHz, CDCl$_3$): δ 3.17–3.44 (m, 2H, CH$_2$NH), 3.45–3.72 (m, 8H, 4CH$_2$ morph.), 3.89 (s, 3H, OCH$_3$), 4.23–4.34 (m, 2H, CH$_2$O cycl.), 4.77 (s, 2H, CH$_2$CO), 6.46 (d, J=1.0 Hz, 1H, Ar), 6.57 (d, J=1.0 Hz, 1H, Ar), 7.97 (s, 1H, CH=N). ^{13}C-NMR (101 MHz, CDCl3): δ 169.7, 151.0, 148.4, 137.6, 133.1, 130.5, 105.7, 102.9, 70.1, 66.41, 65.3, 56.4, 44.5, 38.9. Elemental Analysis calculated for C$_{16}$H$_{21}$N$_3$O$_5$ (Supporting Information Table S13).

(Z)-8-methoxy-3,4-dihydro-2H-benzo[b][1,4]oxazine-6-carbaldehyde O-(2-(2,6-dimethylmorpholino)-2-oxoethyl) oxime 1b. Yield: 94%. ^{1}H-NMR (200 MHz, CDCl$_3$): δ 1.35–1.64 (m, 6H, 2CH$_3$ morph.), 3.39–3.98 (m, 11H, CH$_2$NH+2CH$_2$N morph.+2CHO morph.+OCH$_3$), 4.27–4.53 (m, 2H, CH$_2$O), 4.73–4.90 (m, 2H, CH$_2$CO), 6.47 (s, 1H, Ar), 6.65 (s, 1H, Ar), 8.02 (s, 1H, CH=N). ^{13}C-NMR (101 MHz, CDCl$_3$): δ 169.4, 151.2, 148.3, 137.8, 133.0, 130.6, 105.8, 103.0, 70.2, 69.3, 65.4, 56.3, 52.2, 38.8, 18.0. IR (CHCl$_3$): 3415 (NH), 1711 (CO), 1606 (C=N) cm^{-1}. Elemental Analysis calculated for C$_{18}$H$_{25}$N$_3$O$_5$ (Table S13)

(Z)-8-methoxy-3,4-dihydro-2H-benzo[b][1,4]oxazine-6-carbaldehyde O-(2-(4-hydroxypiperidin-1-yl)-2-oxoethyl) oxime 1c. Yield: 29%. ^{1}H-NMR

(200 MHz, CDCl$_3$): δ 1.41–2.02 (2 m, 4H, 2CH$_2$ pip.), 3.12–3.34 (m, 2H, CH$_2$NH), 3.36–3.53 and 3.64–4.18 (2 m, 8H, OCH$_3$+CHOH+2CH$_2$N pip.), 4.25–4.43 (m, 2H, CH$_2$O cycl.), 4.77 (s, 2H, CH$_2$CO), 6.51 (s, 1H, Ar), 6.62 (s, 1H, Ar), 8.00 (s, 1H, CH=N). ^{13}C-NMR (101 MHz, CDCl$_3$): δ 169.8, 151.1, 148.5, 137.7, 133.0, 131.1, 105.8, 103.0, 70.1, 67.3, 65.4, 56.5, 42.8, 38.8, 34.1. Elemental Analysis calculated for C$_{17}$H$_{23}$N$_3$O$_5$. (Supporting Information Table S13).

General procedure for the synthesis of compounds 2a–b. To a solution of the (Z)-3,4-dihydro-2H-8-methoxy-1,4-benzoxazin-7-car-baldehyde oxime **8** (1.04 g, 5 mmol) in an. DMF (10 mL), NaH (0.5 g of a 60% mineral dispersion, 10 mmol) is added in small portion at 0 °C and the reaction mixture is stirred at room temperature for 2 hours. Then, the suitable choropropionyl amides **12a,b** (15.59 mmol)$^{[31]}$ solved in an. DMF (5 mL) is added and the mixture is stirred at room temperature for 18 hours. After cooling to room temperature, the mixture is poured into H$_2$O (50 mL), extracted with dichloromethane (30×30 mL); the combined organic phases are washed with brine (3×20 mL) and H$_2$O (3×20 mL), dried (MgSO$_4$) and concentrated under reduced pressure. The resulting crude is purified by Silicagel column using as the eluent firstly with diethyl ether, then ethyl acetate, to obtain a yellow oil (**2a**) or a brown solid (**2b**).

(Z)-8-methoxy-3,4-dihydro-2H-benzo[b][1,4]oxazine-6-carbaldehyde O-(3-morpholino-3-oxopropyl) oxime 2a. Yield: 50%. ^{1}H-NMR (200 MHz, CDCl$_3$): δ 2.06 (t, J=4.4 Hz, 2H, CH$_2$CO), 3.31–3.53 (m, 4H, 2CH$_2$N), 3.77–4.02 (m, 9H, 3CH$_2$+OCH$_3$), 4.06–4.23 and 4.30–4.44 (2 m, 4H, 2CH$_2$O), 6.47 (s, 1H, Ar), 6.70 (s, 1H, Ar), 7.98 (s, 1H, CH=N). ^{13}C-NMR (101 MHz, CDCl$_3$): δ 171.0, 151.2, 148.6, 137.7, 133.0, 130.8, 105.8, 103.0, 68.0, 66.4, 65.3, 56.4, 44.2, 38.8, 35.4. Elemental Analysis calculated for C$_{17}$H$_{23}$N$_3$O$_5$ (Supporting Information Table S13).

(Z)-8-methoxy-3,4-dihydro-2H-benzo[b][1,4]oxazine-6-carbaldehyde O-(3-(2,6-dimethylmorpholino)-3-oxopropyl) oxime 2b. Brown solid. M.p.: 140.2–143.1 °C. Yield: 25%. ^{1}H-NMR (200 MHz, CDCl$_3$): δ 2.09–2.64 (m, 6H, 2CH$_3$ morph.), 3.24–3.49 (t, J=4.4 Hz, 2H, CH$_2$CO), 3.53–4.01 (m, 13H, 2CHO morph.+CH$_2$O cycl.+2CH$_2$N+OCH$_3$+CH$_2$NH), 4.21–4.50 (m, 2H, CH$_2$O), 6.71 (d, J=1.4 Hz, 1H, Ar), 6.80 (d, J=1.0 Hz, 1H, Ar), 8.22 (s, 1H, CH=N). ^{13}C-NMR (101 MHz, CDCl$_3$): δ 171.4, 151.1, 148.7, 137.8, 132.9, 130.6, 105.7, 103.0, 69.2, 68.0, 65.3, 56.4, 38.8, 35.4, 18.0. Elemental Analysis calculated for C$_{19}$H$_{27}$N$_3$O$_5$ (Supporting Information Table S13).

General procedure for the synthesis of compounds 3a,b. To a solution of the (Z)-3,4-dihydro-2H-8-methoxy-1,4-benzoxazin-6-carbaldehyde O-(oxiran-2-ylmethyl)oxime **9** (1.32 g, 5 mmol) in an. DMF (7 mL) morpholine or 2,6-dimethylmorpholine is added (42.5 mmol) and the mixture is heated at 50–60 °C for 18 hours. After cooling to room temperature, the mixture is poured into H$_2$O (30 mL), extracted with ethyl acetate (3×30 mL); the combined organic phases are washed with H$_2$O (3×20 mL), dried (MgSO$_4$) and concentrated under reduced pressure. The crude is purified by Silicagel flash chromatography using as the eluents firstly diethyl ether, then a mixture of diethyl ether/methanol (9:1) to obtain a yellow oil.

(Z)-8-methoxy-3,4-dihydro-2H-benzo[b][1,4]oxazine-6-carbaldehyde O-(2-hydroxy-3-morpholinopropyl) oxime 3a. Yield: 30%. ^{1}H-NMR (200 MHz, CDCl$_3$): δ 2.33–2.74 (m, 6H, 3CH$_2$N), 3.10 (br s, 1H, OH, disappears with D$_2$O), 3.31–3.47 (m, 2H, CH$_2$NH), 3.62–3.78 (m, 4H, 2CH$_2$O morph.), 3.87 (s, 3H, OCH$_3$), 4.02–4.40 (m, 5H, 2CH$_2$O+ CHOH), 6.43 (s, 1H, Ar), 6.58 (s, 1H, Ar), 7.92 (s, 1H, CH=N). ^{13}C-NMR (101 MHz, CDCl$_3$): δ 151.2, 149.0, 137.8, 133.0, 130.6, 105.8, 102.9, 75.0, 66.9, 66.3, 65.2, 61.0, 56.4, 54.2, 39.1. Elemental Analysis calculated for C$_{17}$H$_{25}$N$_3$O$_5$ (Supporting Information Table S13).

(Z)-8-methoxy-3,4-dihydro-2H-benzo[b][1,4]oxazine-6-carbaldehyde O-(3-(2,6-dimethylmorpholino)-2-hydroxypropyl) oxime 3b. Yield: 30%.

ChemMedChem | Research Article
doi.org/10.1002/cmdc.202300046

Chemistry
Europe
European Chemical
Societies Publishing

^{1}H-NMR (200 MHz, CDCl$_3$): δ 1.07–1.27 (m, 6H, 2CH$_3$), 2.13–2.96 (3 m, 6H, 3CH$_2$N), 3.34–3.57 (m, 2H, CH$_2$NH), 3.59–3.82 (m, 1H, CHOH), 3.88 (s, 3H, OCH3), 3.96–4.44 (m, 6H, 2CH$_2$O + 2CHO morph.), 6.46 (s, 1H, Ar), 6.61 (s, 1H, Ar), 7.95 (s, 1H, CH=N). ^{13}C-NMR (101 MHz, CDCl$_3$): δ 151.0, 149.0, 138.1, 133.1, 130.6, 105.8, 103.0, 74.8, 70.0, 66.5, 65.4, 60.7, 59.2, 56.3, 38.8, 18.2. IR (CHCl$_3$): 3125–3100 (NH + OH), 1605 (C=N) cm^{-1}. Elemental Analysis calculated for C$_{19}$H$_{29}$N$_3$O$_5$ (Supporting Information Table S13).

Synthesis of (Z)-3,4-dihydro-2H-8-methoxy-1,4-benzoxazin-7-carbalde-hyde O-[2-hydroxy-3-(4-hydroxypiperidin-1-yl)propyl]oxime **3c**. To a solution of the (Z)-3,4-dihydro-2H-8-methoxy-1,4-benzoxazin-6-car-baldehyde O-(oxiran-2-ylmethyl)oxime **9** (1.32 g, 5 mmol) in an. DMF (2 mL) piperidin-4-ol (1 g, 9.82 mmol) is added and the mixture is heated at 50–60 °C for 18 hours. After cooling to room temperature, the mixture is poured into H$_2$O (30 mL), extracted with ethyl acetate (3×30 mL); the combined organic phases are washed with H$_2$O (3×20 mL), dried (MgSO$_4$), and concentrated under reduced pressure. The crude is purified by Silicagel flash chromatography using as eluent diethyl ether to obtain a brown oil. Yield: 26%. ^{1}H-NMR (200 MHz, CDCl$_3$): δ 3.37–3.74 (m, 10H, 4CH$_2$N + CH$_2$NH), 3.79–4.08 (m, 6H, OCH$_3$ + CHOH pip. + CH$_2$N), 4.28–4.56 (m, 5H, 2OCH$_2$ + CHOH), 6.86 (d, J = 1.8 Hz, 1H, Ar), 6.91 (d, J = 1.0 Hz, 1H, Ar), 9.74 (s, 1H, CH=N). ^{13}C-NMR (101 MHz, CDCl$_3$): δ 151.2, 149.0, 138.0, 133.1, 130.6, 105.8, 103.0, 74.7, 67.1, 66.4, 65.4, 60.8, 56.4, 51.0, 39.0, 34.8. Elemental Analysis calculated for C$_{18}$H$_{27}$N$_3$O$_5$ (Supporting Information Table S13).

Molecular docking simulations

All the studied PDE4Is were manually built by the MOE Builder program and then were parametrized (AM1 partial charges as calculation method) and energy minimized by the Energy Minimize Program using MMFF94x forcefield of MOE and RMS (root mean square) gradient equal to 0.0001, being the root mean square gradient the norm of the gradient times the square root of the number of (unfixed) atoms. This allowed to produce a single low-energy conformation for each ligand.[26] All the possible enantiomers had been considered.

All the selected X-ray data of the PDE4 enzyme in presence of different inhibitors had been collected from the Protein Data Bank.[49]

Re-cross docking calculations as well as the following docking runs involving the newly developed in-house PDE4DIs have been performed by means of MOE. Evaluation of the RMSD values between the co-crystallized ligand and the related docking pose has been performed by PyMOL.[28]

As regard the DOCK tool implemented in MOE, the template similarity methodology was applied, choosing as binding site the one occupied by NAP21 (PDB code 5K32) and TCD2 (PDB code 7W4X), or by the references GEBR-32a, GEBR-20b and GEBR-26 g at the PDE4D catalytic site (PDB codes 6FDC, 6F8U and 6F8X, respectively), including all those residues placed 4.5 Å far from the aforementioned inhibitor. This works by placing ligands in the active site based on one or more reference structures (templates). This aligns template and input molecules via an undirected heavy-atom and projected feature triplet matching scheme. The scoring function incorporates terms for reference/ligand similarity as well as a protein-ligand clash term.

Calculation of the enthalpy-based Affinity dG scoring function allowed to score the generated fifty poses while the Induced Fit method has been exploited to refine the previous poses to the final ten docking poses, maintaining the Affinity dG as final scoring function for the definitive pose ranking.

This Affinity dG function estimates the enthalpic contribution to the free energy of binding using a linear function:

$$\Delta G = C_{hb}f_{hb} + C_{ton}f_{ion} + C_{hmlig}f_{mlig} + C_{hh}f_{jj}$$

Where the f terms fractionally count atomic contacts of specific types and the C's are coefficients that weight the term contributions to the affinity estimate. The individual terms are: hb: interactions between hydrogen bond donor-acceptor pairs. An optimistic view is taken; for example, two hydroxyl groups are assumed to interact in the most favourable way; ion ionic interactions. A Coulomb-like term is used to evaluate the interactions between charged groups. This can contribute to or detract from binding affinity; mlig: metal ligation. Interactions between Nitrogens/Sulfurs and transition metals are assumed to be metal ligation interactions; hh: hydrophobic interactions, for example, between alkane carbons. These interactions are generally favourable; hp: interactions between hydrophobic and polar atoms. These interactions are generally unfavourable; aa; an interaction between any two atoms. This interaction is weak and generally favourable.

Induced Fit approach allows to maintain flexible protein sidechains within the selected binding site, which are to be included in the refinement stage. The derived docking poses were prioritized by the score values of the lowest energy pose of the compounds docked to the protein structure, as follows: S: the final score (which herein corresponds to affinity dG), which is the score of the last stage of refinement, E_place: score from the placement stage; E_score1 and E_score2 score from rescoring stages 1 and 2; E_refine: score from the refinement stage, calculated to be the sum of the van der Waals electrostatics and solvation energies, under the Generalized Born solvation model (GB/VI).

The pharmacophore analysis has been derived based on the pharmacophore search module implemented in MOE software. The related pharmacophore consensus tool led to a set of suggested features based on the proposed alignment of inhibitors. In particular, we exploited the docking poses of the selected most potent NAPs, as scored by the MOE Dock scoring functions (S). The pharmacophore requirements are accompanied by a position, radius and a type expression. Details of the applied strategy are described in our previous papers.[45,50,51]

Biological studies

Antioxidant activity on endothelial cells

EAhy926 human endothelial cells (ATCC® CRL-2922™) were cultured in DMEM supplemented with 10% FBS, 1% Glutamine, 1% penicillin/streptomycin.[52] Intracellular ROS production was evaluated on EAhy926 endothelial cells treated with H2O2 by using the CellROX® Deep Red Reagent. Cells were pre-treated in 96-well plates with tested compounds (at 10 μM concentration) for 1 hour prior to H$_2$O$_2$ stimulus (H$_2$O$_2$ 50 μM for 1 hour).

Following incubation with H$_2$O$_2$, CellROX® Reagent was added at a final concentration of 5 μM to the cells.

Cells were incubated for 45 minutes at 37 °C, in the last 15 minutes the live cell nuclear reagent Hoechst 33342 at 1 μg/ml was added, then cells were washed three times with PBS and read at ex/em 620/680 for CellROX® Deep Red Reagent and at ex/em 360/485 for Hoechst 33342 in a Spark multimode microplate Reader (Tecan Italia S.r.l.). Results were evaluated as CellROX to Hoechst fluorescence ratio.

ChemMedChem

Research Article
doi.org/10.1002/cmdc.202300046

**Chemistry
Europe**
European Chemical
Societies Publishing

Antioxidant activity in human platelets: preparative procedures and ROS assay

Freshly drawn venous blood from healthy volunteers of the "Centro Trasfusionale, Ospedale San Martino" in Genoa was collected into 130 mM aqueous trisodium citrate anticoagulant solution (9:1). The donors claimed to have not taken drugs known to interfere with platelet function during two weeks prior to blood collection and gave their informed consent. Washed platelets were prepared centrifuging whole blood at $100 \times g$ for 20 min. The obtained platelet-rich plasma was then centrifuged at $1100 \times g$ for 15 min. Pellet was washed once with pH 5.2 ACD solution (75 mM trisodium citrate, 42 mM citric acid and 136 mM glucose), centrifuged at $1100 \times g$ for 15 min and then re-suspended in pH 7.4 HEPES buffer (145 mM NaCl, 5 mM KCl, 1 mM $MgSO_4$, 10 mM glucose, 10 mM HEPES).

ROS production was quantified as previously reported[53,54] by 2',7'-dichlorofluorescein diacetate (DCFH-DA), a ROS-sensitive probe that yields upon oxidation the fluorescent adduct 2'-7'-dichlorofluorescin (DCF) that is trapped inside the cells. Briefly, washed platelets (1.0×10^8/mL), pre-incubated with saline and compounds **1b**, **3b**, **GEBR-20b** for 15 min at 37 °C, were stimulated by 0.1 U/mL thrombin. Incubation was stopped by cooling samples in ice bath and then samples were immediately analysed in a Merck Millipore Bioscience Guava easyCyte flow cytometer (Merk Millipore, Burlington, MA, USA).

Compounds **1b**, **3b** and **GEBR-20b** were diluted in saline from a stock DMSO solution immediately before each experiment. DCFH-DA, thrombin and all the chemicals were purchased from Sigma-Aldrich/Merck Millipore.

Data and statistical analysis

The reported IC_{50} value is the molar concentration of the tested compound able to obtain 50% inhibition of the maximal activity induced by the stimulation agent (H_2O_2 or thrombin) and it is calculated by the percentage of inhibition that is the inhibition of the maximal activity measured in the presence of the drug compared with that measured in a control sample containing saline, carried out under the same conditions.

Reported data are mean ± SD of three (in endothelial cells) and five (in platelet) independent experiments, each performed at least in triplicate. Statistical comparisons between two groups were made through the unpaired Student's t-test. Statistical significance was defined as $p < 0.05$.

In silico prediction of ADMET properties

The prediction of all the reported ADMET parameters was performed by means of the Advanced Chemistry Development (ACD) Percepta platform (ACD/Percepta Platform; Advanced Chemistry Development, Inc.: Toronto, ON, Canada, 2015).[55] The software prediction is managed based on the implemented training libraries, which refer to different series of derivatives whose pharmacokinetic and safety properties has been experimentally evaluated and reported in the literature. Prediction of PAINS (Pan Assay Interference structures) and of the compound putative biological target(s) was performed via SwissADME website[46] and SwissTarget,[47] respectively.

Supporting Information

Table S1: Residues lining the active site of PDE4B and PDE4D. Table S2. The PDE4-GEBR complexes analysed by X-ray diffraction. Table S3: Chemical structure and biological activity of the most effective TCDs derivatives. Table S4. List of the five best scored docked poses obtained for TCDs as performed by the MOE Dock module at the 7W4X PDB code. Table S5: Chemical structure and biological activity as PDE4Is of the most effective NAPs. Table S6: Chemical structure and biological activity of the most effective NAPs. Table S7: List of the five best scored docked poses obtained for NAPs. Table S8: Molecular structure and biological activity as PDE4Is of the most potent NAPs. Table S9: List of the five best scored docked poses obtained for GEBR20b, GEBR-26 g and GEBR-32a as performed by the MOE Dock module at the 6FDC PDB code. Table S10: List of the five best scored docked poses obtained for GEBR-20b, GEBR-26 g and GEBR-32a as performed by the MOE Dock module at the 6F8X PDB code. Table S11: List of the five best scored docked poses obtained for GEBR-20b, GEBR-26 g and GEBR-32a as performed by the MOE Dock module at the 6F8U PDB code. Table S12: List of the five best scored docked positioning obtained for the herein newly developed putative PDE4D inhibitors 1–3, performed by the MOE Dock module at the 6F8U PDB code. Table S13: Elemental analysis of compounds 1–9. Figure S1: X-ray crystallographic pose of GEBR-32a at the human PDE4D. Figure S2: X-ray crystallographic pose of GEBR-20b at the human PDE4D. Figure S3: X-ray crystallographic pose of GEBR-26 g at the human PDE4D. Figure S4: Ligplot of the zwitterion tautomer docking pose of the PDE4I TCD23a. Figure S5: X-ray crystallographic pose of NAP21 within the PDE4D catalytic site. Figure S6: Pharmacophore features exhibited by NAPs are reported, in tandem with their related distances Figure S7: Comparison of 6FDC with the 6F8U and 6F8X PDB codes. Figure S8: Comparison of the newly developed GEBR series with the pharmacophore model herein developed. Figure S9:^{1}H NMR (400 MHz) of (Z)-3,4-dihydro-2H-8-methoxy-1,4-benzoxazin-6-carbaldehyde oxime 8. Figure S10:^{13}C NMR (101 MHz) of (Z)-3,4-dihydro-2H-8-methoxy-1,4-benzoxazin-6-carbaldehyde oxime 8. Figure S11: IR spectrum of compound 8. Figure S12: ^{1}H-NMR ($CDCl_3$, 200 MHz) of compound 9. Figure S13: ^{13}C-NMR (101 MHz) of compound 9. Figure S14: IR spectrum of compound 9. Figure S15:^{1}H-NMR ($CDCl_3$, 200 MHz) of compound 1a. Figure S16: ^{13}C-NMR (100 MHz) of compound 1a. Figure S17: ^{1}H-NMR ($CDCl_3$, 200 MHz) of compound 1b. Figure S18: ^{13}C-NMR (101 MHz) of compound 1b. Figure S19: IR spectrum of compound 1b. Figure S20:^{1}H-NMR ($CDCl_3$, 200 MHz) of compound 1c. Figure S21: ^{13}C-NMR (101 MHz) of compound 1c. Figure S22: ^{1}H-NMR ($CDCl_3$, 200 MHz) of compound 2a. Figure S23: ^{13}C-NMR (101 MHz) of compound 2a. Figure S24: ^{1}H-NMR ($CDCl_3$, 200 MHz) of compound 2b. Figure S25: ^{13}C-NMR (101 MHz) of compound 2b. Figure S26: ^{1}H-NMR ($CDCl_3$, 200 MHz) of compound 3a. Figure S27: ^{13}C-NMR (101 MHz) of compound 3a. Figure S28: ^{1}H-NMR ($CDCl_3$, 200 MHz) of compound 3b. Figure S29: ^{13}C-NMR (101 MHz) of compound 3b. Figure S30: IR spectrum of compound 3b. Figure S31: ^{1}H-NMR ($CDCl_3$, 200 MHz) of compound 3c. Figure S32: ^{13}C-NMR

ChemMedChem

Research Article
doi.org/10.1002/cmdc.202300046

Chemistry
Europe
European Chemical
Societies Publishing

(101 MHz) of compound 3c. Figure S33. Figure S34: ^{1}H-NMR (DMSO-d_6, 200 MHz) of known intermediate 5. Figure S34: Prediction of putative target preferences featured by the PDE4 inhibitors Apremilast and Rolipram.

Conflict of Interest

The authors declare no conflict of interest.

Data Availability Statement

The data that support the findings of this study are available on request from the corresponding author.

[1] A. D. Bondarev, M. M. Attwood, J. Jonsson, V. N. Chubarev, V. V. Tarasov, W. Liu, H. B. Schiöth, *Front. Pharmacol.* **2022**, *13*, 1057083.

[2] J. E. Phillips, *Front. Pharmacol.* **2020**, *11*, 259.

[3] M. A. Schick, N. Schlegel, *Int. J. Mol. Sci.* **2022**, *23*, 120910.

[4] A. J. Tibbo, G. S. Baillie, *Cells* **2020**, 1254, doi: 10.3390/cells9051254.

[5] D. Singh, S. Lea, A. G. Mathioudakis, *Drugs* **2021**, *81*, 1821–1830.

[6] S. Lea, A. Metryka, J. Li, A. Higham, C. Bridgewood, G. Villetti, M. Civelli, F. Facchinetti, D. Singh, *Cytokine* **2019**, *123*, 154739.

[7] N. Moretto, P. Caruso, R. Bosco, G. Marchini, F. Pastore, E. Armani, G. Amari, A. Rizzi, E. Ghidini, R. De Fanti, C. Capaldi, L. Carzaniga, E. Hirsch, C. Buccellati, A. Sala, C. Carnini, R. Patacchini, M. Delcanale, M. Civelli, G. Villetti, F. Facchinetti, *J. Pharmacol. Exp. Ther.* **2015**, *352*, 559–567.

[8] J. Distel, S. Cazzaniga, S. M. Seyed Jafari, V. Emelianov, C. Schlapbach, N. Yawalkar, K. Heidemeyer, *Dermatology* **2022**, *238*, 267–275.

[9] M. Schepers, D. Paes, A. Tiane, B. Rombaut, E. Piccart, L. van Veggel, P. Gervois, E. Wolfs, I. Lambrichts, C. Brullo, O. Bruno, E. Fedele, R. Ricciarelli, C. Ffrench-Constant, M. E. Bechler, P. van Schaik, W. Baron, E. Lefevere, K. Wasner, A. Grünewald, C. Verfaillie, P. Baeten, B. Broux, P. Wieringa, N. Hellings, J. Prickaerts, T. Vanmierlo, *Brain Behav. Immun.* **2022**, *109*, 1–22.

[10] R. S. Roberts, S. Sevilla, M. Ferrer, J. Taltavull, B. Hernández, V. Segarra, J. Gràcia, M. D. Lehner, A. Gavaldà, M. Andrés, J. Cabedo, D. Vilella, P. Eichhorn, E. Calama, C. Carcasona, M. Miralpeix M, *J. Med. Chem.* **2018**, *61*, 2472–2489.

[11] R. Zhang, H. Li, X. Zhang, J. Li, H. Su, Q. Lu, G. Dong, H. Dou, C. Fan, Z. Gu, Q. Mu, W. Tang, Y. Xu, H. Liu, *Eur. J. Med. Chem.* **2021**, *211*, 113004.

[12] J. R. Hedde, A. N. Hanks, C. J. Schmidt, Z. A. Hughes, *Brain Behav. Immun.* **2017**, *64*, 285–295.

[13] D. Paes, M. Schepers, B. Rombaut, D. van den Hove, T. Vanmierlo, J. Prickaerts, *J. Pharmacol. Rev.* **2021**, *73*, 1016–1049.

[14] T. Peng, B. Qi, J. He, H. Ke, J. Shi, *J. Med. Chem.* **2020**, *63*, 10594–10617.

[15] G. L. Card, B. P. England, Y. Suzuki, D. Fong, B. Powell, B. Lee, C. Luu, M. Tabrizizad, S. Gillette, P. N. Ibrahim, D. R. Artis, G. Bollag, M. V. Milburn, S. H. Kim, J. Schlessinger, K. Y. J. Kam Zhang, *Structure* **2004**, *12*, 2233–2247.

[16] C. Brullo, M. Massa, C. Villa, R. Ricciarelli, D. Rivera, M. A. Pronzato, E. Fedele, E. Barocelli, S. Bertoni, L. Flammini, O. Bruno, *Bioorg. Med. Chem.* **2015**, *23*, 3426–3435.

[17] C. Brullo, R. Ricciarelli, J. Prickaerts, O. Arancio, M. Massa, C. Rotolo, A. Romussi, C. Rebosio, B. Marengo, M. A. Pronzato, B. T. van Hagen, N. P. van Goethem, P. D'Ursi, A. Orro, L. Milanesi, S. Guariento, E. Cichero, P. Fossa, E. Fedele, O. Bruno, *Eur. J. Med. Chem.* **2016**, *124*, 82–102.

[18] R. Ricciarelli, C. Brullo, J. Prickaerts, O. Arancio, C. Villa, C. Rebosio, E. Calcagno, M. Balbi, B. T. J. van Hagenc, E. K. Argyrousic, H. Zhang, M. A. Pronzato, O. Bruno, E. Fedele, *Sci Rep* **2017**, *7*, 46320, doi: 10.1038/srep46320.

[19] T. Prosdocimi, L. Mollica, S. Donini, M. S. Semrau, A. P. Lucarelli, E. Aiolfi, A. Cavalli, P. Storici, S. Alfei, C. Brullo, O. Bruno, E. Parisini, *Biochemistry* **2018**, *57*, 2876–2888.

[20] F. Zhou, Y. Yue Huang, L. Liu, Z. Song, K. Q. Hou, Y. Yang, H. B. Luo, Y. Y. Huang, X. F. Xiong, *Biochem. Pharmacol.* **2022**, *202*, 115123.

[21] O. Bruno, C. Brullo, N. Arduino, S. Schenone, A. Ranise, F. Bondavalli, L. Ottonello, P. Dapino, F. Dallegri, *Il Farmaco* **2004**, *59*, 223–235.

[22] X. Bingtian, Q. Yunyun, L. Dan, C. Ningbo, W. Jinling, J. Lan, J. Limei, Z. Zhongzhen, X. Jiangping, W. Haitao, *Redox Biol.* **2020**, *28*, 101342.

[23] T. T. Lin, Y. Y. Huang, G. H. Tang, Z. B. Cheng, X. Liu, H. B. Luo, S. Yin, *J. Nat. Prod.* **2014**, *77*, 955–962.

[24] Z. Song, Y. Y. Huang, K. Q. Hou, L. Liu, F. Zhou, Y. Huang, G. Wan, H. B. Luo, X. F. Xiong, *J. Med. Chem.* **2022**, *65*, 4238–4254.

[25] M. D. Woodrow, S. P. Ballantine, M. D. Barker, B. J. Clarke, J. Dawson, T. W. Dean, C. J. Delves, B. Evans, S. L. Gough, S. B. Guntrip, S. Holman, D. S. Holmes, M. Kranz, M. K. Lindvaal, F. S. Lucas, M. Neu, L. E. Ranshaw, Y. E. Solanke, D. O. Somers, P. Ward, J. O. Wiseman, *Bioorg. Med. Chem. Lett.* **2009**, *19*, 5261–5265.

[26] Molecular Operating Environment (MOE); Chemical Computing Group ULC, 1010 Sherbooke St. West, Suite #910, Montreal, QC, Canada, H3 A 2R7, 2021. Available online: http://www.chemcomp.com/.

[27] D. Ramírez, J. Caballero, *Molecules* **2018**, *23*, 1038.

[28] The PyMOL Molecular Graphics System, Version 1.2r3pre, Schrödinger, LLC.

[29] I. A. Pearl, D. L. Beyer, *J. Org. Chem.* **1951**, *17*, 217–220.

[30] K. Koshi, M. Shimizu, *Chem. Pharm. Bull.* **1978**, *17*, 2343–2350.

[31] H. Eshghi, M. H. Alizadeh, E. Davamdar, *J. Korean Chem. Soc.* **2008**, *52*, 52–57.

[32] C. Brullo, M. Massa, M. Rocca, C. Rotolo, S. Guariento, D. Rivera, R. Ricciarelli, E. Fedele, P. Fossa, O. Bruno, *J. Med. Chem.* **2014**, *57*, 7061–7072.

[33] X. Chen, C. Guo, J. Kong, *Neural. Regen. Res.* **2012**, *7*, 376–385.

[34] M. C. Haigis, B. A. Yankner, *Mol. Cell.* **2010**, *40*, 333–344.

[35] G. K. Hansson, P. Libby, I. Tabas, *J. Intern. Med.* **2015**, *278*, 483–493.

[36] C. Brullo, M. Massa, F. Rapetti, S. Alfei, M. B. Bertolotto, F. Montecucco, M. G. Signorello, O. Bruno, *Molecules* **2020**, *25*, 899.

[37] R. J. Haslam, N. T. Dickinson, E. K. Jang, *Thromb. Haemostasis* **1999**, *82*, 412–423.

[38] C. D. Wright, P. J. Kuipers, D. Kobbylarz-Singer, L. J. Devall, B. A. Klinkefus, R. E. Weishaar, *Biochem. Pharmacol.* **1990**, *40*, 699–707.

[39] M. Bevilacqua, T. Vago, G. Baldi, E. Renesto, F. Dallegri, G. Norbiato, *Eur. J. Pharmacol.* **1994**, *268*, 415–423.

[40] C. H. Coyle, L. J. Martinez, M. C. Coleman, D. R. Spitz, N. L. Weintraub, K. N. Kader, *Free Radical Biol. Med.* **2006**, *40*, 2206–2213.

[41] H. Van de Waterbeemd, E. Gifford, *Nat. Rev. Drug Discovery* **2003**, *2*, 192–204.

[42] M. Tonelli, S. Espinoza, R. R. Gainetdinov, E. Cichero, *Eur. J. Med. Chem.* **2017**, *127*, 781–792.

[43] D. F. Veber, S. R. Johnson, H. Y. Cheng, B. R. Smith, K. W. Ward, K. D. Kopple, *J. Med. Chem.* **2002**, *45*, 2615–2623.

[44] C. A. Lipinski, F. Lombardo, B. W. Dominy, P. J. Feeney, *Adv. Drug Delivery Rev.* **2001**, *46*, 3–26.

[45] E. Cichero, A. Calautti, V. Francesconi, M. Tonelli, S. Schenone, P. Fossa, *Pharmaceuticals* **2021**, *14*, 1307.

[46] D. Gfeller, O. Michielin, V. Zoete, *Bioinformatics.* **2013**, *29*, 3073–3079.

[47] A. Daina, O. Michielin, V. Zoete, *Nucl. Acids Res.* **2019**, *47*, W357–W364.

[48] C. Brullo, F. Rapetti, S. Abbate, T. Prosdocimi, A. Torretta, M. Semrau, M. Massa, S. Alfei, P. Storici, E. Parisini, O. Bruno, *Eur. J. Med. Chem.* **2021**, *223*, 113638.

[49] H. M. Berman, T. Battistuz, T. N. Bhat, W. F. Bluhm, P. E. Bourne, K. Burkhardt, Z. Feng, G. L. Gilliland, L. Iype, S. Jain, *Acta Crystallogr. Sect. D* **2002**, *58*, 899–907.

ChemMedChem

Research Article
doi.org/10.1002/cmdc.202300046

Chemistry
Europe
European Chemical
Societies Publishing

[50] G. Righetti, M. Casale, M. Tonelli, N. Liessi, P. Fossa, N. Pedemonte, E. Millo, E. Cichero, *Pharmaceuticals* **2020**, *13*, 445.

[51] G. Righetti, M. Tonelli, P. Fossa, E. Cichero, *Med. Chem.* **2021**, *17*, 1151–1165.

[52] P. Altieri, R. Murialdo, C. Barisione, E. Lazzarini, S. Garibaldi, P. Fabbi, C. Ruggeri, S. Borile, F. Carbone, A. Armirotti, M. Canepa, A. Ballestrero, C. Brunelli, F. Montecucco, P. Ameri, P. Spallarossa, *Br. J. Pharmacol.* **2017**, *174*, 3713–3726.

[53] G. Leoncini, M. Maresca, C. Colao, *Biochem. Int.* **1991**, *25*, 647–655.

[54] M. Maresca, C. Colao, G. Leoncini, *Cell Biochem. Funct.* **1992**, *10*, 79–85.

[55] www.acdlabs.com (accessed on July 2022).
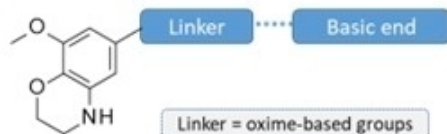
RESEARCH ARTICLE

Novel 1-3 compounds as anti-inflammatory agents

Basic end = morpholine- and piperidine-based groups

Linker ···· Basic end

Linker = oxime-based groups

Prof. E. Cichero, Dr. F. Rapetti, Dr. M. Lusardi, Dr. N. Scarano, S. Alfei, P. Altieri, S. Garibaldi, P. Ameri, M. Grazia Signorello, Prof. C. Brullo*

1 – 17

Scouting Different Phosphodiesterase 4 Inhibitor Chemotypes in Silico To Guide the Design of Anti-inflammatory/Antioxidant Agents

Based on the X-ray data of previous phosphodiesterase 4 (PDE4) inhibitors, compounds **1–3** were designed, synthesized, and screened in silico as putative PDE4 inhibitors to exploit structural variation at the catechol group to gain further contacts, especially with the flat aromatic residues of PDE4. Subsequent in vitro biological assays on platelets and endothelial cells provided evidence for antioxidant and anti-inflammatory activity.